DESIGN AND TESTING OF A FOUR-BAR FLAPPING WING MECHANISM

A THESIS SUBMITTED TO
THE GRADUATE SCHOOL OF NATURAL AND APPLIED SCIENCES
OF
MIDDLE EAST TECHNICAL UNIVERSITY

BY

MÜNİRE GÜLAY ŞENOL

IN PARTIAL FULFILLMENT OF THE REQUIREMENTS
FOR
THE DEGREE OF MASTER OF SCIENCE
IN
AEROSPACE ENGINEERING

FEBRUARY 2016

Approval of the thesis:

DESIGN AND TESTING OF A FOUR-BAR FLAPPING WING MECHANISM

Submitted by **MÜNİRE GÜLAY ŞENOL** in partial fulfillment of the requirements for the degree of **Master of Science in Aerospace Engineering Department, Middle East Technical University** by,

Prof. Dr. Gülbin Dural Ünver _____
Dean, Graduate School of **Natural and Applied Sciences**

Prof. Dr. Ozan Tekinalp _____
Head of Department, **Aerospace Engineering**

Assoc. Prof. Dr. D. Funda Kurtuluş _____
Supervisor, **Aerospace Engineering Dept., METU**

Examining Committee Members:

Prof. Dr. Ozan Tekinalp _____
Aerospace Engineering Dept., METU

Assoc. Prof. Dr. Dilek Funda Kurtuluş _____
Aerospace Engineering Dept., METU

Asst. Dr. Nilay Sezer Uzol _____
Aerospace Engineering Dept., METU

Asst. Prof. Dr. Ali Türker Kutay _____
Aerospace Engineering Dept., METU

Asst. Prof. Dr. Kutluk Bilge Arıkan _____
Mechatronic Engineering Dept., Atılım University

Date: 04.02.2016

I hereby declare that all information in this document has been obtained and presented in accordance with academic rules and ethical conduct. I also declare that, as required by these rules and conduct, I have fully cited and referenced all material and results that are not original to this work.

Name, Last name: Münire Gülay Şenol

Signature:

ABSTRACT

DESIGN AND TESTING OF A FOUR-BAR FLAPPING WING MECHANISM

Şenol, Münire Gülay

M.S., Department of Aerospace Engineering

Supervisor: Assoc. Prof. Dr. Dilek Funda Kurtuluş

February 2016, 79 pages

The purpose of this thesis is to design and test a flapping wing four-bar mechanism. A four-bar linkage system kinematic analysis is introduced for flapping wing motion. The type of mechanism is double rocker and the motion has a single-degree of freedom. Four-bar mechanism is activated by a servo motor which is driven by microcontroller. From the design of four bar mechanism, two different simulations result two different flapping angles and flapping frequencies. This thesis provides a detailed description of the design and manufacturing of the flapping mechanism and its experimental setup. The wing has pure flapping motion with fixed incidence angle. Force measurements are performed for hover modes by using a force transducer. CFD analyses are performed for both hover and forward flight cases. The numerical and experimental results are discussed and compared.

Keywords: Flapping Wing Mechanism, Four-Bar Mechanism, Computational Fluid Dynamics, Force Measurement, Micro Air Vehicles, Unsteady Aerodynamics

ÖZ

DÖRT ÇUBUK ÇIRPAN KANAT MEKANİZMASI TASARIMI VE TESTİ

Şenol, Münire Gülay
Yüksek Lisans, Havacılık ve Uzay Mühendisliği Bölümü
Tez Yöneticisi: Doç. Dr. Dilek Funda Kurtuluş

Şubat 2016, 79 sayfa

Bu tezin amacı çırpan kanatlı dört-çubuk mekanizmasının tasarlanması ve deney çalışmasının yapılmasıdır. Dört-çubuk mekanizma sisteminin kinematik analizi çırpan kanat hareket denklemi kullanılarak yapılmıştır. Çift sarkaç mekanizması kullanılmış olup hareket bir serbestlik derecesine sahiptir. Dört çubuk mekanizması aktivasyonu için mikrodenetleyici ile sürülen servo motor kullanılmıştır. Bu dört çubuk mekanizması tasarımında iki farklı simülasyondan iki farklı çırpma açısısı ve iki farklı çırpma frekansı ortaya çıkmıştır. Bu tezde mekanizmanın tasarımı, üretimi ve deneysel düzenek detaylı olarak tarif edilmektedir. Kanat sabit hücüm açısıyla çırpma hareketi yapmaktadır. Sensör kullanarak havada asılı kalma durumu için kuvvet ölçümleri yapılmıştır. Havada asılı kalma ve ileri uçuş durumları için hesaplamalı akışkanlar dinamiği analizleri yapılmıştır. Sayısal ve deneysel sonuçlar tartışılmış ve karşılaştırılmıştır.

Anahtar Kelimeler: Çırpan Kanat Mekanizması, Dört-Çubuk Mekanizması, Hesaplamalı Akışkanlar Dinamiği, Kuvvet Ölçümü, Mikro Hava Aracı

To my mother, father and sister…

ACKNOWLEDGEMENTS

I would like to thank my advisor, Assoc. Prof. Dr. Dilek Funda Kurtuluş for her support, guidance, patience, knowledge and suggestions during all my study. She always encouraged me and I could be able to complete this study.

I would like to express my thanks to fellow friend Tuğba Pişkin. She is always there for me during my university life. She is always special friend for me.

I would like to say thank to İclal Alev Değim and Ebru Küzay. They believe I will achieve. They always show their love to me.

I thank my labmate and project mate, Fadile Yudum Çömez who is always there to help me. I also thank my school friends, Ali, Berk, Erkan, Gökhan, Hasan, Ömer and Muharrem for their helps and supports.

A special thanks goes to Demircan and Arzu, who gave original idea about my design.

I would also like to thank my family. My mother Nuran Şenol, my father Fuat Şenol and my sister Nurhan Nuray Şenol always provided me, loved me. Without whose love, encouragement and support, I could not finish my thesis.

I offer thanks to The Scientific and Technological Council of Turkey (TÜBİTAK 213M327) and TUBA GEBIP Award 2012-18 for financial support during my thesis.

TABLE OF CONTENTS

LIST OF TABLES

TABLES

LIST OF FIGURES

FIGURES

CHAPTER 1

INTRODUCTION

1.1 Background Information

Micro aerial vehicles (MAVs) which are a class of unmanned air vehicle (UAVs) have raised in value to accomplish commercial, research (aerial photography), government, and military purposes (policing) in the past decade. MAVs get access dangerous and inaccessible region easier than other vehicles. MAVs which are used indoor and outdoor activities, have limited size; wingspan should be equal or smaller than 15 cm [1].With advancing micro technology, working on MAVs gain speed and importance. MAVs are characterized with their small sizes, low weights and moveable. There are three kind of MAVs; fixed wing, rotary wing and flapping wing.

Flapping wing MAVs have gained inspiration for long years in natural flyers such as insects and birds. Flying insects and birds can fly differently such as, hovering, perching, gliding and soaring by changing the pitch angle, feather orientation, flying trajectory, direction of motion and wing area. Furthermore, they can fly at low speeds and also take-off and land at very short time. Especially insects fly at low speeds however flap their wings at high flapping frequencies.

Leonardo da Vinci whose inspiration sources are bats and birds drew the first flying machines with flapping wings in the 15^{th} century (Figure 1.1) [2]. In the last two decades, with developing technology, many scientists sticks to design and generate of flapping wing MAVs. Flapping wing MAVs are usually used for indoor activities. They ensure more excellent, complex and fast maneuverability than fixed or rotary

wing aircrafts. In addition, unlike other MAVs, flapping wing MAVs can fly in hover mode and glide mode.

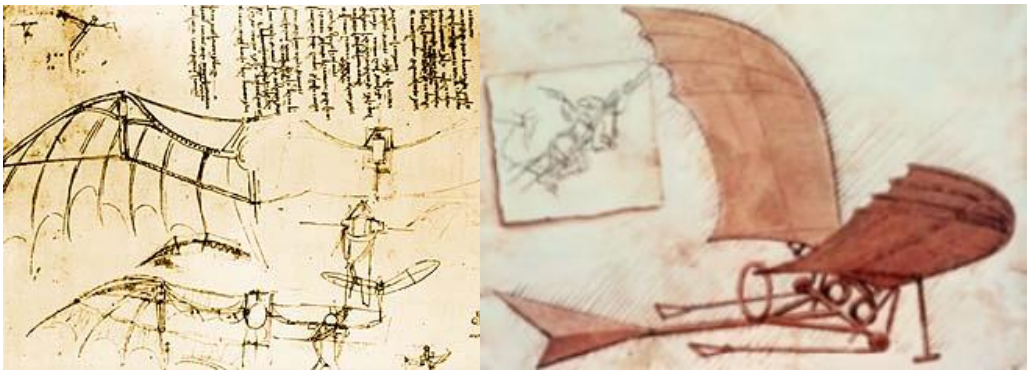

Figure 1.1 Drawing of a flying machine (left) and a glider (right) of Leonardo da Vinci [2]

1.2 Objectives and Thesis Outline

The objective of this study is,

- to investigate different four-bar mechanisms used for MAV applications
- to design and test a four-bar flapping wing mechanism
- to compare experimental data from the force/torque sensor and computational fluid dynamics results

In the present work, four-bar flapping mechanism with rigid wing is designed and manufactured. Mechanism which can perform a done pure sweep motion is tested with 6-axis force/torque sensor (case 1&2). The mechanism kinematics, flapping frequency and forces parameters are investigated. 3D CFD analysis are carried out for hover cases (case 1&2) and for forward flight case (case 2). When input angle is 10°, 41.5° flapping angle is obtained at 11.2 Hz (case 1); when input angle is 20°, 85.9° flapping angle is obtained at 5.85 Hz (case 2). Computational and experimental results are compared.

- Chapter 1 includes background information about micro air vehicles, major objectives and future studies.
- Chapter 2 expresses the literature survey, types of four mechanism MAVs which have motor driven four-bar mechanisms and piezo-driven four-bar mechanisms.
- Chapter 3 initiates the kinematic of wing and four-bar flapping mechanism.
- Chapter 4 describes the experimental analysis. In this chapter, the manufacturing of the mechanism, the experimental setup, and the experimental results are shown.
- Chapter 5 defines the numerical analysis. 3D CFD analysis are done with Ansys-Fluent.
- Chapter 6 gives conclusion of the current study.

CHAPTER 2

LITERATURE SURVEY

Different mechanisms are introduced in literature for flapping wing micro air vehicles. Most of the researches in literature are observed to use DC motors (brushless or brushes) or servos ([4-11]) as a driver of a flapping wing mechanism. Gears and different types of four bar mechanisms are also widely used in flapping wings designs ([4-11]).

2.1 Four-Bar Mechanism

The mechanisms comprise of moving parts which one of them can convert or transform input forces and generate some functional motions to the other parts as output forces and motions [3]. There are various forms of mechanisms which are used for different purposes. The most widely used and simplest mechanism is a four-bar mechanism which is a closed chain mechanism. This type of mechanisms have four rotating joints and four links (one of them fixed and the others are movable). The fixed link is called a frame which is immobilized with base revolute joint. The other links are connected with rotating joint to each other and they have two diversified movement. The crank makes full spin about fixed link; on the other hand, rocker swings between two limiting angles depending on the length of the links. There is no connection between coupler link and fixed link (Figure 2.1).

There are three different types of four-bar mechanisms. The first one is double crank four-bar mechanism, two links make full spin about the fixed axis. In this type mechanism, the shortest link is fixed link (Figure 2.2a). The second type is double-

rocker four-bar mechanism whose two links make a partial rotation with limited angles. The shortest link is l_2 or l_3 (Figure 2.2b). The last type is a crank-rocker mechanism, one link can full spin and the other one swings with limited angles. In crank-rocker mechanism, the shortest link is l_1 or l_3. The crank mechanism has also two different types. The crank is the driver link and the rotary motion is converted to an oscillatory motion (Figure 2.2c). In the second one the rocker is the driver link, the oscillatory motion is converted to a rotary motion (Figure 2.2d). Double-crank and crank-rocker mechanism's motion are continuous motions; on the other hand double rocker mechanism's motion are limited to some angles [3].

Depending on the length of the links, motion characteristics and limiting angles of mechanism can be different from the other ones. Suitable length of the links are determined in order to enable a workable mechanism.

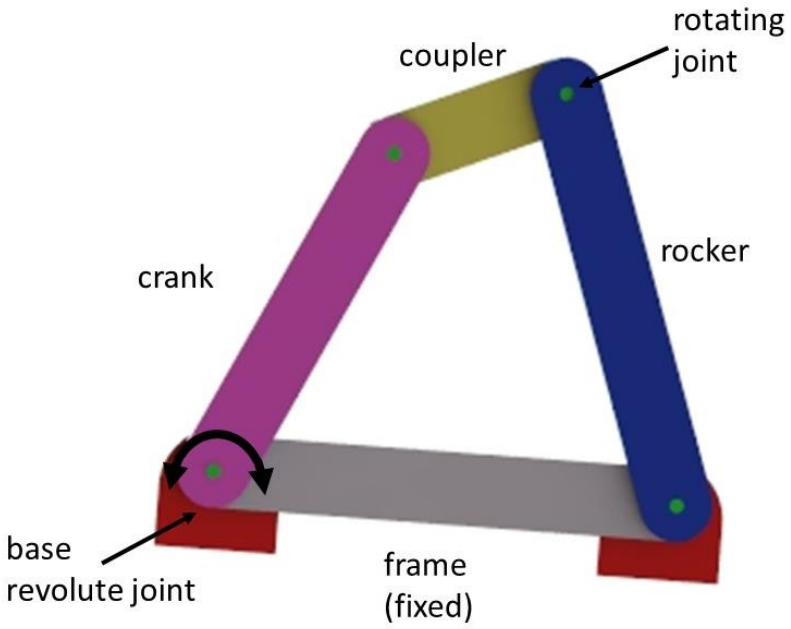

Figure 2.1 Four-bar mechanism

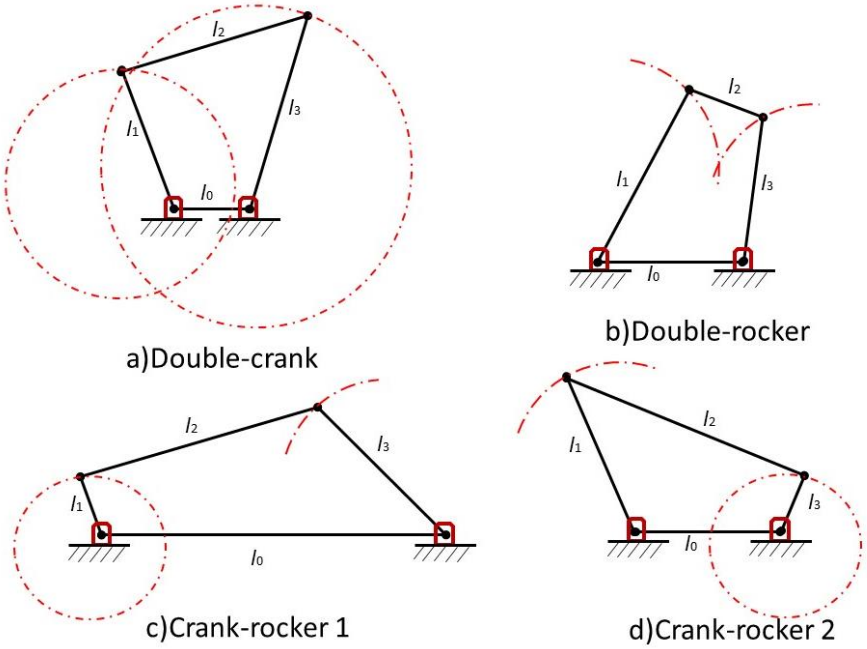

Figure 2.2 Types of four-bar mechanism

Figure 2.3 shows the links and the angles for four-bar mechanism. A_0 and B_0 are fixed points and l_0 is a fixed link. A and B are movable points. Input angle (θ_1) which is an independent variable is the angle between l_0 and l_1 and the output angle (θ_3) is the angle between l_3 and horizontal axis. θ_2 and θ_3 are dependent variables.

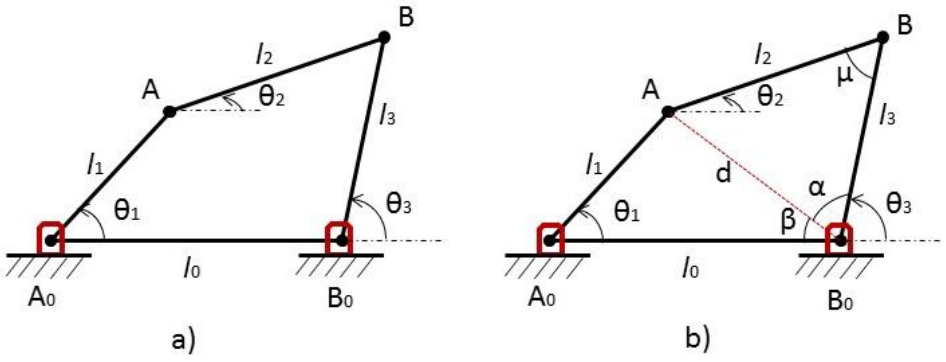

Figure 2.3 Links and angles of four-bar mechanism

Four-bar mechanism can be analyzed by using "Raven's Method" [3]. Using input angle and length of links, the position analysis can be done. For the geometrical analysis, AA_0B_0 triangle is composed and the unknown side of triangle is called d (Figure 2.3b). Applying cosine theorem, dimension of d is calculated and then β angle can be found (Eqs. 2.1-2.2).

$$|d|^2 = l_0^2 + l_1^2 - 2l_0 l_1 \cos(\theta_1) \tag{2.1}$$

$$\beta' = \cos^{-1}\left[\frac{(l_0^2 + d^2 - l_1^2)}{2l_0 d}\right] \quad \beta = \pi - \beta' \tag{2.2}$$

By using triangle ABB_0, using the cosine theorem, the unknown variables θ_2 and θ_3 can be found (Eqs. 2.3-2.4).

$$\alpha = \cos^{-1}\left[\frac{(l_3^2 + d^2 - l_2^2)}{2l_3 d}\right] \quad \theta_3 = \pi - (\alpha + \beta) \tag{2.3}$$

$$\mu = \pm\cos^{-1}\left[\frac{(l_2^2 + l_3^2 - l_2^2)}{2l_0 d}\right] \quad \theta_2 = \theta_3 - \mu \tag{2.4}$$

The position analysis of movable points are done with Eq. 2.5 which is called loop closure equation [3].

$$A_0A + AB = A_0B_0 + B_0B \tag{2.5}$$

$$l_1 e^{i\theta_1} + l_2 e^{i\theta_2} = l_0 + l_3 e^{i\theta_3} \tag{2.6}$$

Eq. 2.6 can be decomposed into written x and y components (Eqs. 2.7-2.8).

$$l_1 \cos\theta_1 + l_2 \cos\theta_2 = l_0 + l_3 \cos\theta_3 \tag{2.7}$$

$$l_1 \sin\theta_1 + l_2 \sin\theta_2 = l_3 \sin\theta_3 \tag{2.8}$$

2.2 Motor-Driven Four-Bar Flapping Mechanisms

In Microbat MEMS Project, Pornsin-Sirirak et al.[4] produced a flapping wing using a four-bar (double pushrod) mechanism with a small 30 Hz DC motor. MEMS technology is used for manufacturing of different types of wings (beetle, dragonfly, bat, butterfly and so on) by using different materials (silicon MEMs, titanium-alloy metal and parylene-C). Two types of power sources are used separately, one of them is super capacitor and the other one is battery. This design is tested in a low-speed wind tunnel. Lift and drag coefficients are examined according to different wing types as flexible and rigid.

Bejgerowski et al. [5] used 65° flap angle with maximum 12.1 Hz flapping frequency using a DC pager motor and gears for their flapping wing design. Their flapping mechanism which is made of polymer is common crank four-bar type. This design has a wingspan of 25 cm and total mass of 12.76 g.

Takahashi et al.'s [6] design which is inspired from hawkmoth (Manduca sexta) is traced from a common crank four-bar with 52° flap angle and 13 Hz flapping frequency using motor and lithium batteries. Wingspan is 25 cm and total mass of the vehicle is 6.8 g. Measurements of pressure coefficient are done by using MEMS pressure sensor chip.

Sahai et al. [7] designed a crank-rocker mechanism with maximum 90° flapping angle. Flapping-wing micro air vehicle has two four-bar transmission mechanism one for each wing. Compact body design is composed of carbon fiber panels and rods, flexure joints, dowel pins and motor. Trust versus power experimentally measurement are investigated in comparison with small and large wing.

Yılmaz [8] have fabricated flapping wing micro aerial vehicle with four-bar mechanism which is activated by micro DC motors and gears. DC motors are controlled with MotorBee microcontroller. Flapping amplitudes are 65°, 100° and 135° at 10 Hz flapping frequency. Mechanism components are fabricated by using a 3D printer.

Seshadri et al. [9] intended two different four-bar mechanism; one of these mechanisms has 1 DOF fixed-pitch flapping motion and the other one can do 3 DOF motion; namely flapping, pitching and coning. Rigid rectangular wing with 8 inch span is used. They used different measurement techniques.

One of the recent study by National University of Singapore exposed a DC brushless motor and gears with 1 degree of freedom crank-rocker four-bar mechanism. Mechanism has 130° stroke angle at 10 Hz flapping frequency. DC motor and servos are operated by electronic speed controller (ESC) and battery (lithium polymer) as a power source. Total mass of design is 14.6 grams and wingspan is 22 cm [10].

Recently, Mayo et al. [11] have study on experimental and computational analysis of rigid flapping wings. 1 DOF four-bar mechanism is used, the motion is a pure sinusoidal flap motion with a fixed-pitch angle. Mechanism is activated by a motor and also the angular position is measured by a potentiometer. Flapping amplitude is ±40° and flapping frequencies are 4, 6, 8, 10 Hz. CFD analysis is done and also PIV tests are performed.

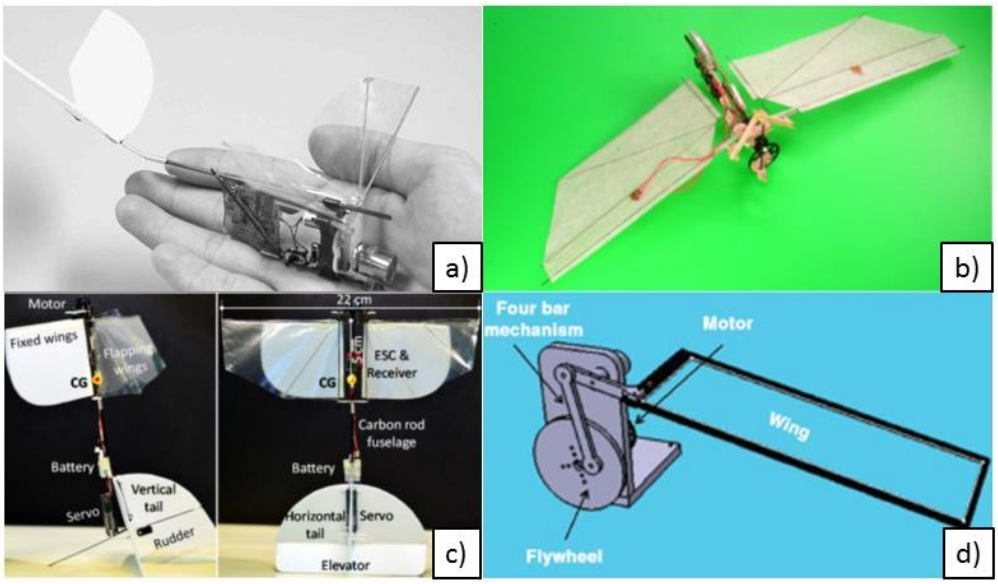

Figure 2.4 Different types of motor-driven four-bar mechanisms [4,6,10,11]

Table 2.1 Different motor-driven four-bar flapping mechanisms

Ref	Flapping Angle [°]	Frequency [Hz]	Weight [g]	Type of Mechanism	Wingspan [cm]
4	-	30	10.5	Four-bar	15
5	65	12.1	12.76	Common crank four-bar	25
6	52	13	6.8	Common crank four-bar	25
7	90	-	15	Crank-rocker four-bar	36
8	65. 100, 135	10	14.6	Four-bar	13
9	120	3	-	Four-bar	20.32
10	130	10	14.6	Crank-rocker four-bar	22
11	80	4,6,8,10		Crank-rocker four-bar	12.7

2.3 Piezo-Driven Four-Bar Flapping Mechanism

In recent years with developing smart material, there exist some applications of flapping wings by using both piezoelectric actuators and four-bar mechanisms.

Mechanical design of flapping wings requires high performance by using light materials. In recent years, some researchers also designed some mechanisms with piezoelectric ceramic material (PZT). PZT is a smart material which converts electric energy to mechanical behavior and it is an ideal material for small sized systems due to high power density, high efficiency, low cost, compact size and weight [12]. However, owing to the fact that PZT has limited bending motion, in the sense of mechanism design, usually double-rocker four-bar mechanism is used to provide suitable flapping angle ([13]-[21]).

One of the earlier studies which has used piezo-driven four-bar mechanism is Micromechanical Flying Insect (MFI) by Fearing et al.[13]. MFI flaps at 17 Hz with ±60° stroke angle by unimorph PZT5H. Shape of four-bar mechanism looks like a triangle. Mass of the total structure is 43 mg. In MFI, two four-bar mechanisms are used to activate only one wing, at the same time, two piezo actuator are used for one four-bar. Wings are made from thick polyester.

Cox et al.[14] have fabricated three four-bar and a five-bar flapping mechanisms by using PZT unimorph actuators. In the first design, four-bar mechanism with carbon-fiber wings can reach 30° flapping angle at 20 Hz by using unimorph PZT (6.3x1.2 cm). The total weight of prototype is 5.5 g. In the other design with four-bar mechanism, two PZT actuator (9.6x2.5 cm) drives the mechanism. It operates at 18 Hz with 50° flapping angle. The wings are made of polymer membrane and carbon fiber spar. This prototype has a weight of 22.8 g. On the other hand, for the same mechanism, using same PZT dimension (6.3x1.2 cm) as the first design, 50° stroke angle at 13 Hz is obtained.

Similarly, researchers of Konkuk University have made a flapping wing system with actuator named as LIPCA (Lightweight Piezo-Composite Actuator) [15], [16], [17] and [18]. Their system is denoted to reach approximately 80° flapping angle by LIPCA with 9 Hz natural flapping frequency. They have two mechanisms for two wings. The flapping device weight is approximately 20g [15]. In addition, they altered wing structure and the four-bar system to reach 92° flapping angle at 17 Hz [16]. Furthermore, using different manufacturing techniques of piezo-composite actuator,

their flapping angle amplitude is obtained to be 110° for original LIPCA and 130° for compressed LIPCA [17].

Another flapping wing prototype was manufactured by Anderson et al. [20]. They created simple four-bar mechanism and used a PZT bimorph cantilever actuator. This mechanism supplied 120° wing stroke amplitude at 30 Hz flapping frequency. Flapping motion is 1 DOF.

A recent study by Lindholm [21] implemented a bimorph piezoelectric actuator with single DOF four-bar mechanisms, where ±55° stroke angle at 30 Hz flapping frequency is obtained.

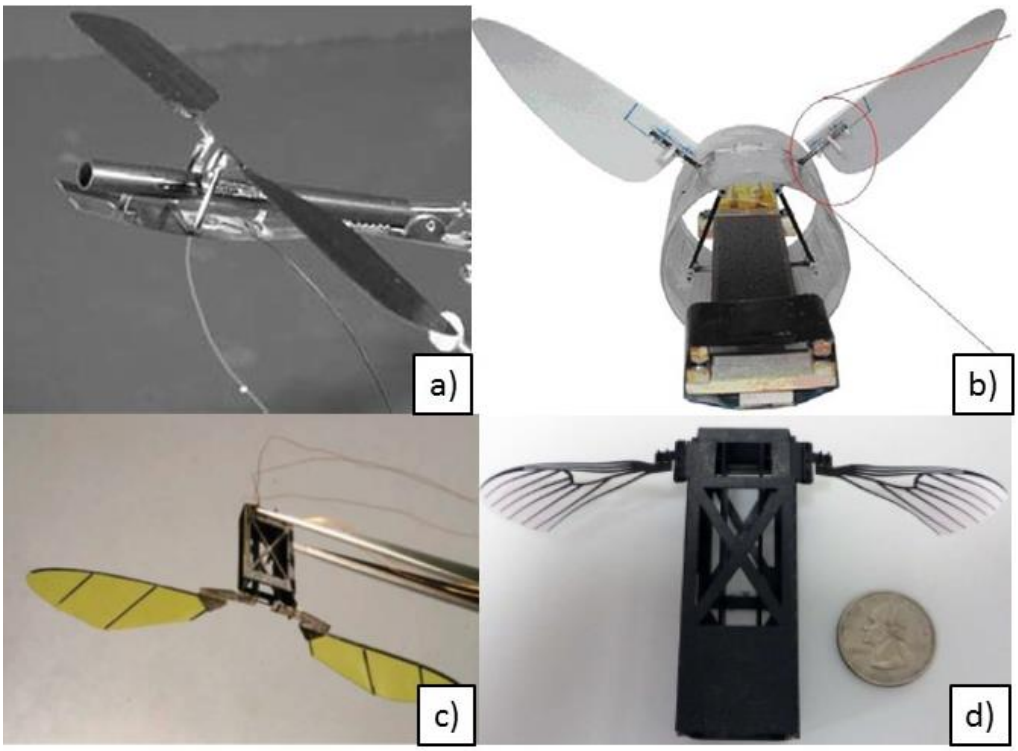

Figure 2.5 Different types of piezo-driven four-bar mechanisms [14, 15, 20, 21]

Table 2.2 Different piezo-driven four-bar flapping mechanisms

Ref	Flapping Angle [°]	Frequency [Hz]	Weight [g]	Type of Mechanism	Piezoelectric Material
13	120	17	0.043	Four-bar	PZT-unimorph
14	30	20	5.5	Four-bar	PZT-unimorph
	50	18	22.8	Four-bar	
	50	13	6.3	Four-bar	
	30	20.5	7	Five-bar	
15	80	9	20	Double-rocker four-bar	PZT-unimorph
16	90	10	19.1	Double-rocker four-bar	PZT-unimorph
17	130	9	-	Double-rocker four-bar	PZT-compressed unimorph
18	92	17	9.6	Double-rocker four-bar	PZT-unimorph
19	100	10	10.28	Double-rocker four-bar	PZT-unimorph
20	120	30	0.35	Slider-crank four-bar	PZT-bimorph
21	110	30	-	Four-bar	PZT-bimorph

CHAPTER 3

FOUR-BAR FLAPPING MECHANISM

In this chapter, the development of flapping wing four-bar mechanism is presented. The geometric definitions of mechanism, kinematic analysis of four-bar and wing are performed using a code written in Matlab.

3.1 Kinematic Analysis of Mechanism

The current flapping mechanism has one fixed (link l_0) and three moving links (l_1, l_2, l_3). The type of four bar mechanism is double-rocker. l_1 and l_3 are rocker, l_2 is coupler bar. Link 0 which is frame bar is placed between A_0 and B_0 points and a rotational motion with a single-degree of freedom is given to the fixed point A_0 (0,0). A_0 and B_0 points are on the same perpendicular line. Coordinates of the A and B points are founded by using Eqs. 3.1-3.2.

$$A_x = l_1(-\sin\theta_1) \qquad A_y = l_1(\cos\theta_1) \tag{3.1}$$

$$B_x = B_{0x} + l_3(\sin\theta_3) \qquad B_y = B_{y0} - l_3(\cos\theta_3) \tag{3.2}$$

The angles θ_1, θ_2, θ_3 and diagonal vector ($\overrightarrow{AB_0}$) are described as shown in Figure 3.1.

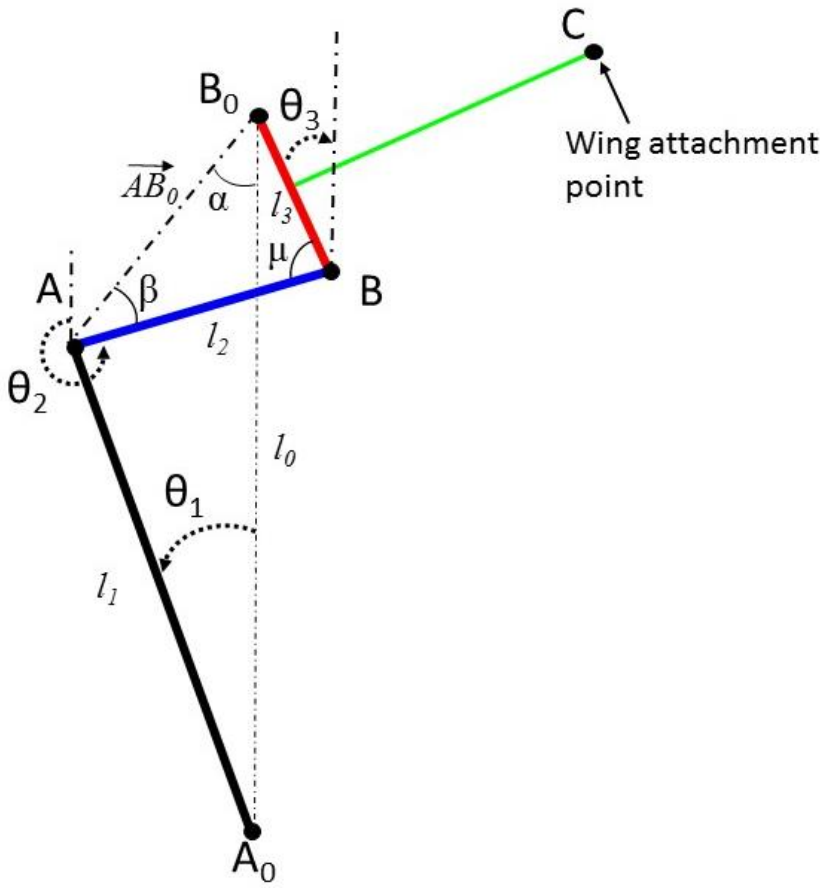

Figure 3.1 Flapping mechanism linkage system

The magnitude of diagonal vector ($|\overrightarrow{AB_0}|$) is calculated using the cosine rule by Eq. 3.3 [15]. θ_1 is the input (driving) angle between Link 0 and Link 1 which is the driving link and θ_3 is the output angle between Link 3 and perpendicular line. In the current study, the angle between link 3 which is the shortest link and wing attachment is taken to be 90°, therefore alteration of flap angle is equal to alteration of θ_3.

$$\left|\overrightarrow{AB_0}\right|^2 = l_0^2 + l_1^2 - 2l_0 l_1 \cos(\theta_1) \tag{3.3}$$

Three angles are defined as α, β and μ as shown in Figure 3.1 to calculate θ_2 and θ_3.

$$\alpha = arccos\left(\frac{l_1^2 + l_0^2 + \overrightarrow{|AB_0|}^2}{2\overrightarrow{|AB_0|}l_0}\right) \tag{3.4}$$

$$\beta = arccos\left(\frac{-l_3^2 + \overrightarrow{|AB_0|}^2 + l_2^2}{2\overrightarrow{|AB_0|}l_0}\right) \quad (3.5)$$

$$\mu = arccos\left(\frac{-\overrightarrow{|AB_0|}^2 + l_2^2 + l_3^2}{2l_1l_3}\right) \quad (3.6)$$

$$\theta_2 = 360 - \beta - \alpha \quad (3.7)$$

$$\theta_3 = 180 - \beta - \alpha - \mu \quad (3.8)$$

In the current study a similar four-bar mechanism is designed as Konkuk University [15]. According to Ref. [15], the size of links are l_1=3 cm, l_2=0.8 cm and l_3=0.75 cm. There is no any information about the length of l_0 in this reference. Using these geometric definitions of the mechanism, kinematic and dynamic analysis are performed using a code written in Matlab 2014a [25] and then l_0 is taken to be 3.8 cm to ensure correct operation of four bar. The length of the bars have an accurate limit in order to obtain workable mechanism. For the current design, input angle, θ_1, can sweep maximum between 1° and 21° so that a $\Delta\theta_1$=20° maximum deflection can be obtained. Otherwise, since the current design is not suitable for full rotation, the four bar mechanism can rotate in a limited range between these angles. The analysis are carried out for 2 different $\Delta\theta_1$ values namely, 10° (1st case) and 20° (2nd case). Figure 3.2 shows the input angle (θ_1) versus output angle (θ_3) of flapping mechanism. When driving angle is 10°, the flapping angle, ϕ, (which is also equal to the output angle θ_3) is changed by 41.5°. When driving angle is 20° at its maximum, the maximum flapping angle change is obtained as $\Delta\varphi$=85.9°

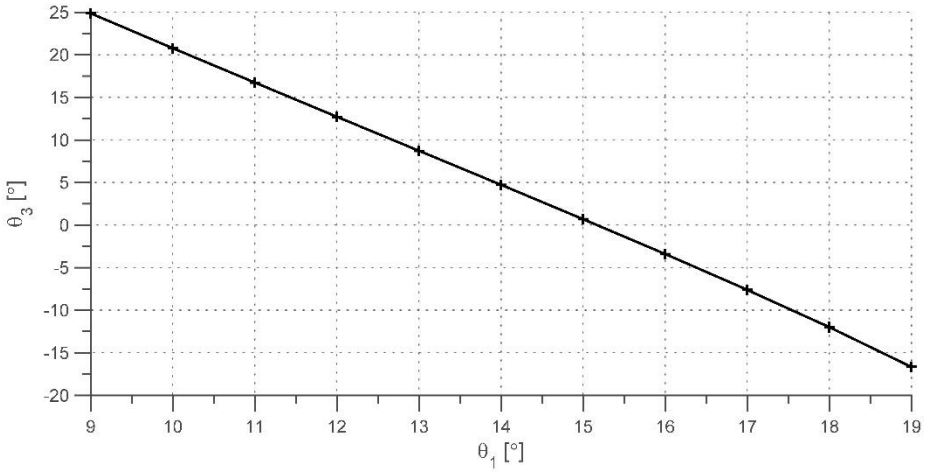

a)1st case

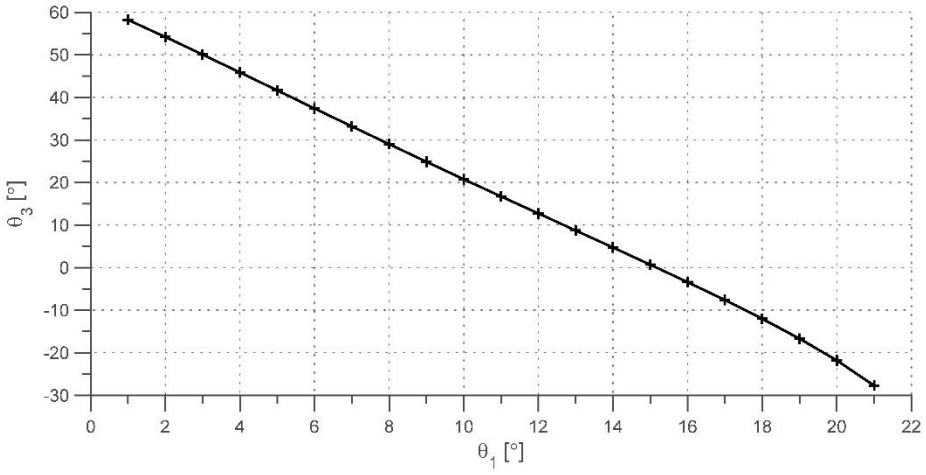

b)2nd case

Figure 3.2 Input angle vs. output angle of flapping mechanism

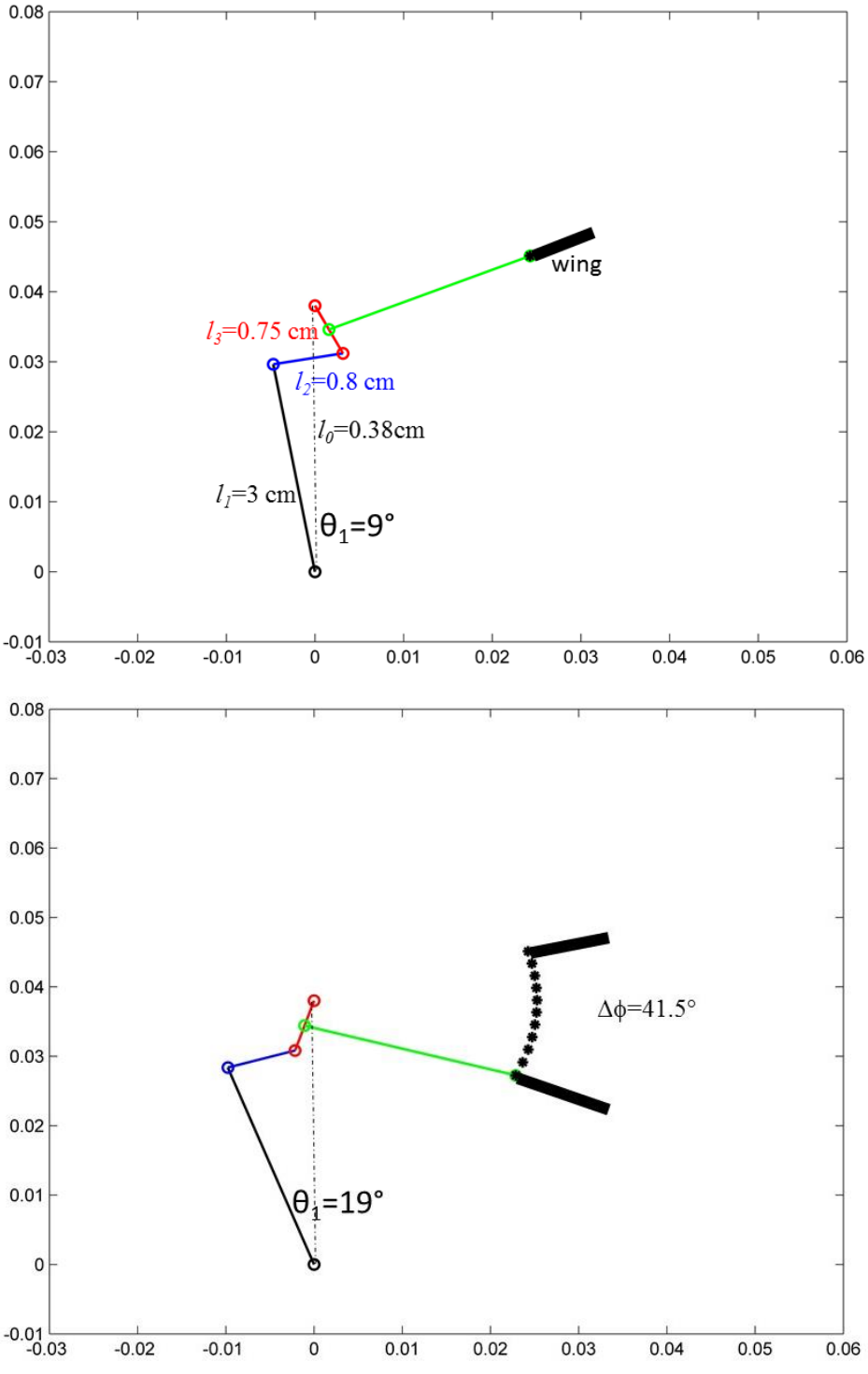

a) 1st case: Input: $\Delta\theta_1$=10°; Output: $\Delta\phi$=41.5°

Figure 3.3 Motion of the flapping four-bar mechanism

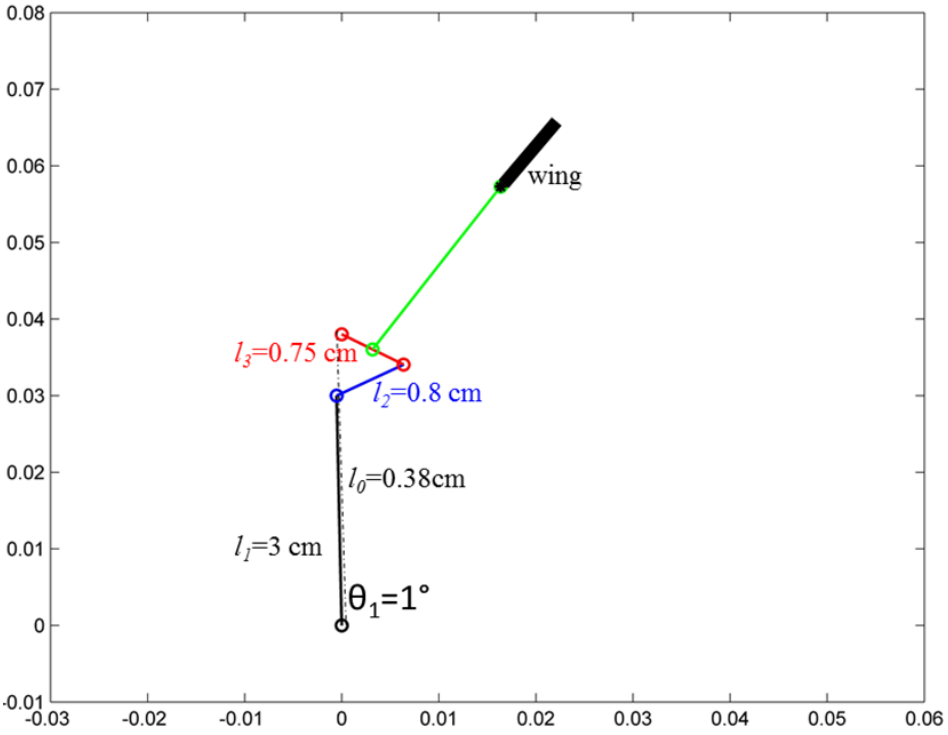

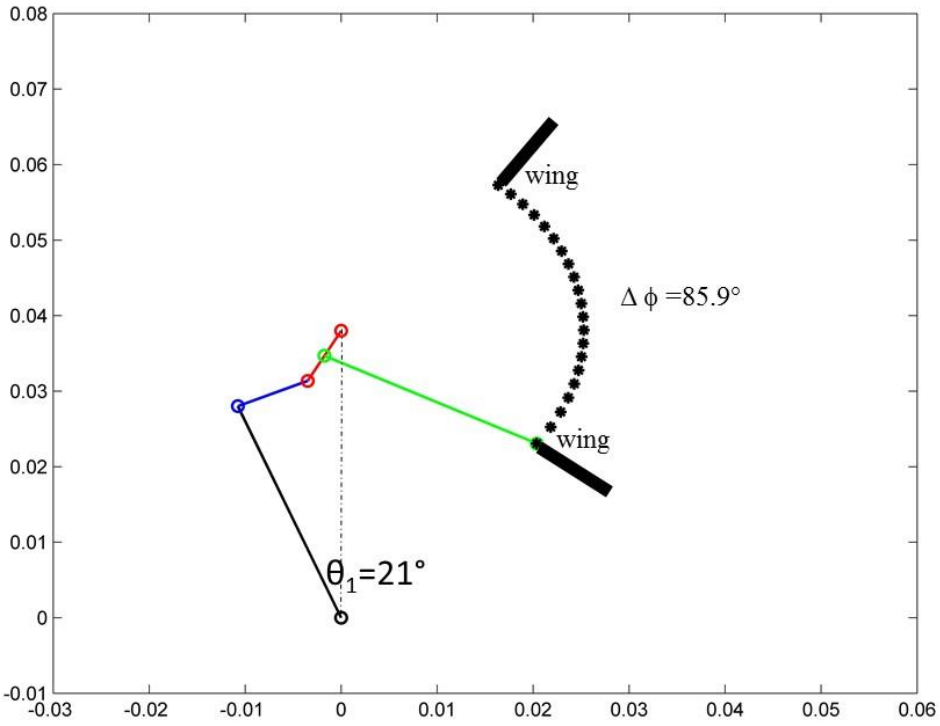

b) 2nd case: Input: $\Delta\theta_1$=20°; Output: $\Delta\phi$=85.9

Figure 3.4 (cont'd)

Link 1 is driven by a servo motor shaft, the flapping motion is an arcing motion (Figure 3.4).

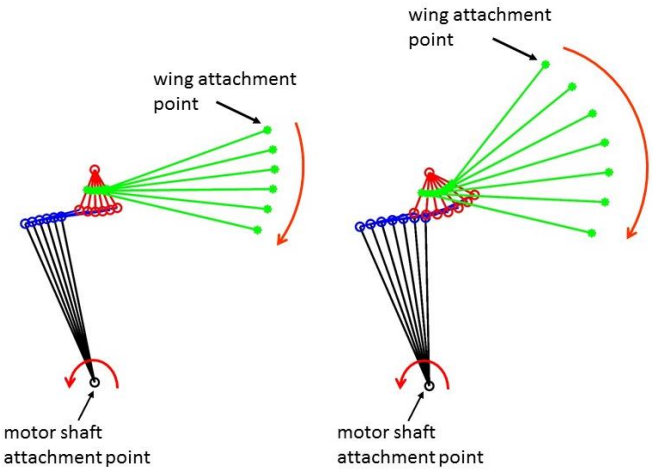

Figure 3.5 Four-bar linkage position in one flapping period

Link 3 (B_0B) which rotates about a fixed point B_0 and the wing attachment which is connected to the center of a link 3 are perpendicular to each other, the wing motion resembles to an arc (Figure 3.5). Wing attachment length is actually 3.5 cm. The coordinates of the wing attachment point (C_x,C_y) is determined by using Eqs. 3.9-3.10.

$$C_x = B_x + \frac{l_3}{2}(-\sin\theta_3) + l_{attachment}(\cos\theta_3) \tag{3.9}$$

$$C_y = B_y + \frac{l_3}{2}(\cos\theta_3) + l_{attachment}(\sin\theta_3) \tag{3.10}$$

where C_x, C_y are x coordinate and y coordinate of point C.

In the first case, at the beginning of the motion, the angle between the wing attachment and the horizontal line is 24.9°; on the other hand, at the end of the motion, the angle between the wing attachment and horizontal line is 16.6°. In the second case, at the beginning of the motion, the angle between the wing attachment and horizontal line is 58.2°; on the other hand, at the end of the motion, the angle between the wing attachment and horizontal line is 27.7°. The angular displacement of the wing attachment are calculated by the code written in Matlab.

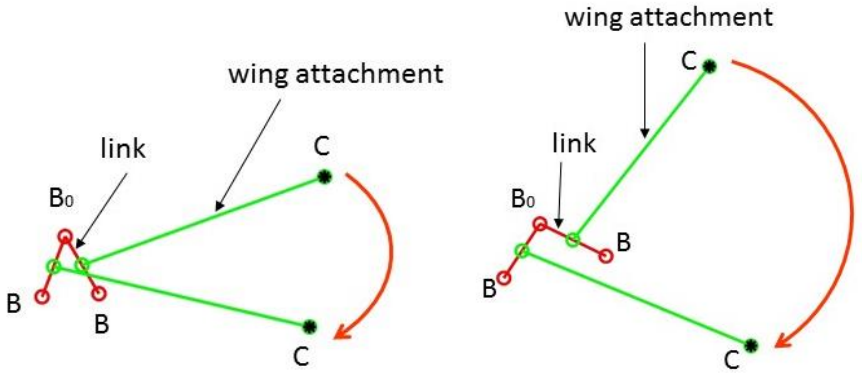

(a) 1st case (b) 2nd case

Figure 3.6 Illustration of the position of the wing attachment at the beginning and end at the of the motion

3.2 Wing Kinematics

The wing is fixed from the wing root to the four bar mechanism with an incident angle (0°), therefore the wing can pure flap (only moving up and down) with no wing rotation (fixed pitch angle & 1 DOF motion). Fixed point B_0 is the origin of the wing coordinate system. Schematic view of the wing coordinate system is shown in Figure 3.6. The angle between the wing and the x axis is called flapping angle (ϕ) which is tracked at the root of the wing. In Figure 3.6, the incidence angle of the wing is 0°. Pitch angle is constant during the experiment.

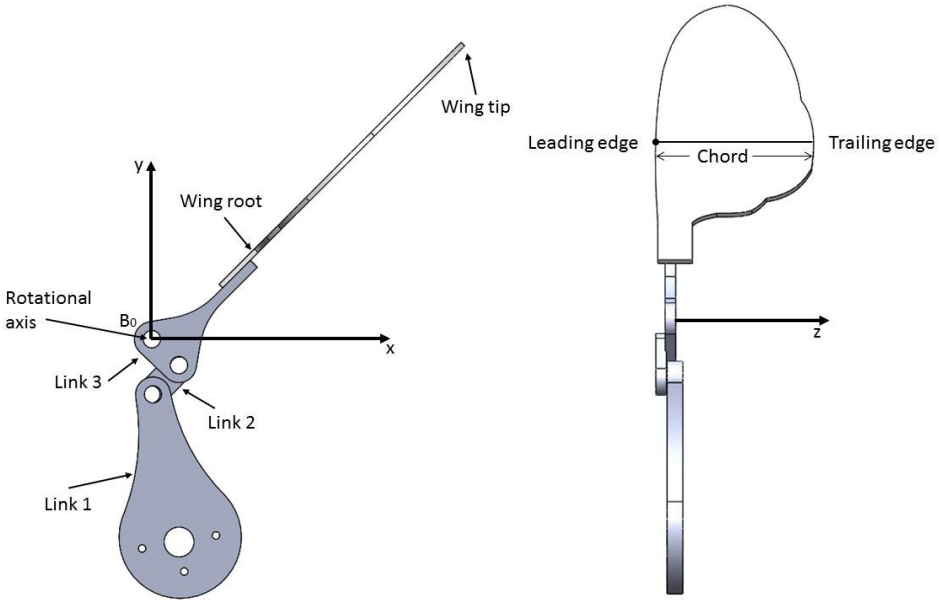

Figure 3.7 Changing of Schematic view of the flapping axis

The wing motion can be defined as a sinusoidal function dependent of time and frequency (Eq. 3.7).

$$\phi(t) = \mathrm{A} * \sin(2\pi f t) \qquad (3.7)$$

In Eq. 3.7, ϕ is the flapping angle, A is the flapping amplitude, *f* is frequency of the system and *t* is time.

CHAPTER 4

EXPERIMENTAL SETUP AND RESULTS

In this chapter, manufacturing and experimental method is presented. There are five main components of flapping mechanism; namely wing, four-bar mechanism, servo motor, Arduino Uno Microcontroller and support stand of mechanism. Fabrication and experiments are done in the Aerospace Engineering Department of METU. Mechanism is activated with servo motor by the help of Arduino Uno Microcontroller. During the experiments, ATI Nano17 F/T sensor is used to measure the unsteady forces and moments. Using a MATLAB code, the data is analyzed.

4.1 Manufacturing of the system

3D CAD drawing of the mechanism are created with Solidworks Software (Figure 4.1). Following the assembly of all parts, every individual part is transformed to 2D technical drawing in order to manufacture the parts using laser cutting machine (Ayka Laser Technology with Phsoft 7.01 program) in Hangar Building of Aerospace Engineering Department. Four bar mechanism parts are cut from 2 mm thick plexiglass plate. The linkages are interconnected to each other by ball bearing with 4 mm outside diameter, 1.5 mm bore diameter. They are also connected with 1.5 mm steel rods. Ball bearings are fixed to the bars with super glue and steel rods are attached with snap rings in order to prevent dislocation.

A support stand is designed to fix the first bar of four-bar mechanism. This four-bar support stand also provides housing for servo-motor. The rod passing across this stand provides a support for the four bar mechanism. The box shaped frame provides a rigid

support for the motion of the mechanism. The support stand is manufactured from 3 mm thick Plexiglass plate (Figure 4.1). In addition, a test stand is designed to provide a base for ATI Nano 17 together with four bar support stand. ATI Nano 17 coordinate system is shown in Figure 4.2. Similarly, test stand is also manufactured from 3 mm plexiglass plate. Plexiglass components are fixed together using chloroform.

The flapping wing used in the current study a similar wing which is an insect wing, namely blow fly (Calliphora Erythocephala) is designed as Konkuk University [19]. The wing has 29.15 mm wing width (chord) and 58.47 mm wing length defines as length from root to tip (Figure 4.3b). The wing area is approximately 1375.27 mm^2. In Table 4.1, Calliphora Erythocephala's morphological parameters [23] and fabricated wing's parameters are shown. The wing is cut from 1 mm thick plexiglass plate and fixed from the wing root to the four bar mechanism with 0° incident angle.

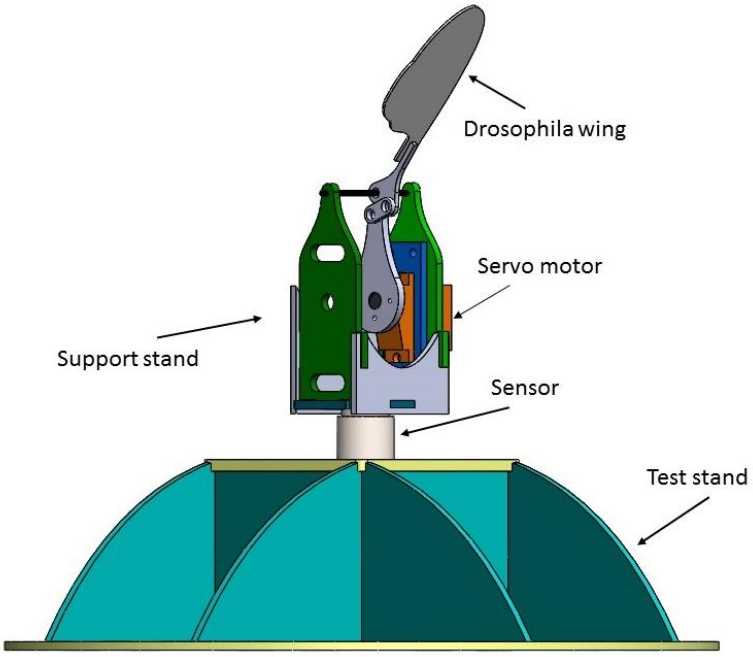

Figure 4. 1 CAD drawing of the experimental setup

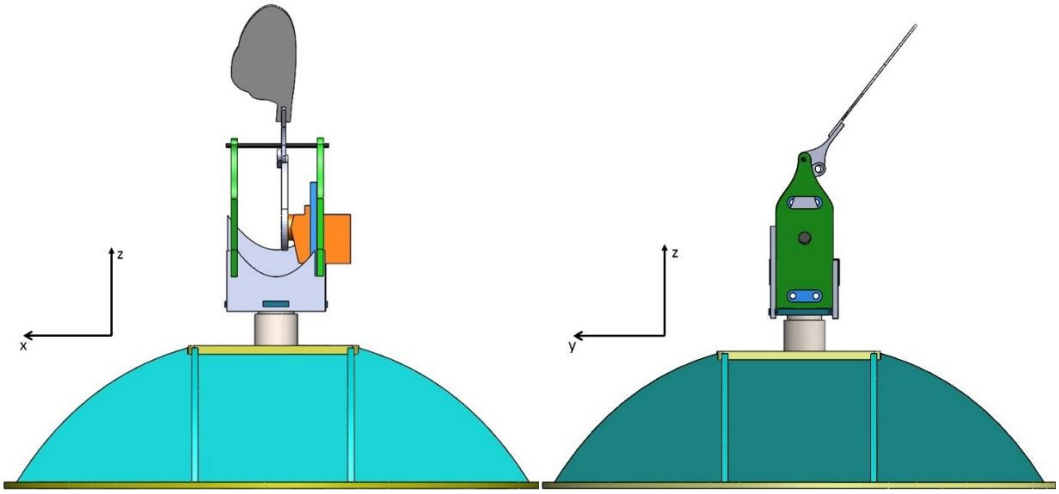

Figure 4. 2 Sensor coordinate system

Table 4. 1 Calliphora Erythocephala's wing morphological parameters [23] and fabricated wing's parameters

Parameters		Calliphora Erythocephala [23]	Calliphora Fabricated Wing
Single wing area [mm^2]	S	29.2	1375.27
Single wing length [mm]	L	9.83	58.47
Chord [mm]	c	2.97	29.15

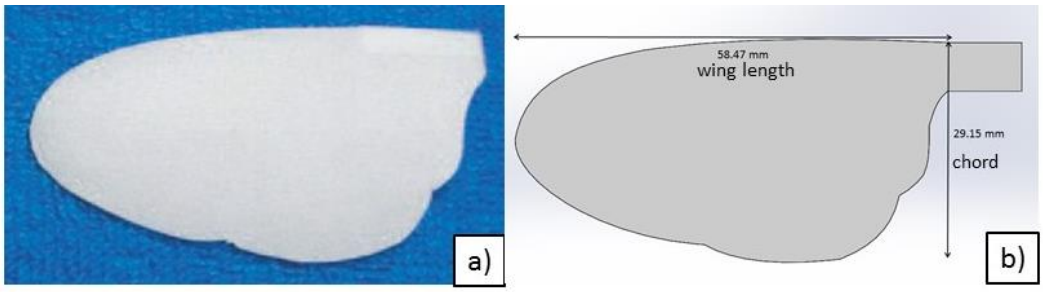

Figure 4. 3 Konkuk University's wing (a) [19] and CAD drawing of Calliphora(b)

4.2 Actuator

Flapping mechanism is activated with servo motor (ART-Tech mini Servo AS-100) (Table 4.2). Motor shaft is combined to linkage 1 to ensure activation. In order to control the servo motor, the Arduino Uno, a microcontroller is used. The servo motor has three wires. One of these wire is the servo power wire takes power from the Arduino outputs 5V. The other cords to ground of Arduino. Last one connects to signal pin in order to read code. The code is written by Arduino language based on C/C++. The code ensures the 10° and 20° sinusoidal motion like go and return back with 1° increments.

Figure 4. 4 Arduino Uno Microcontroller

Table 4. 2 Servo motor specifications

Voltage [V]	4-6
Weight [g]	9
Torque [kg/cm]	1.2
Speed [sec/60]	0.12
Dimensions [mm]	22.5x12x27

4.3 Experimental Setup

One of the challenges of flapping wing micro air vehicles is the measurement of the small aerodynamic forces and moments. Force and torque are measured by using 6-axis sensor ATI Nano17. The current force/torque sensor has resolution of 3 mN of thrust and 16 μNm of moment. Ati DAQ F/T card (FTIFPS1) establishes connection between the sensor and National Instruments DAQ card. A National Instruments DAQ card with a 16 inputs, 16-bit multifunction X series (X1USB-6361) is transformed from analog signal to digital signals. Measurements are recorded at a sampling rate at 1000 Hz by using Labview program. The experimental setup is shown in Figure 4.5.

4.3.1 Force and Torque Measurement

Ati Nano17 F/T sensor has been preferred because of its ability of measuring too small force and torque in six-axis. Measurements are recorded at a sampling rate at 1000 Hz for all experiments. Labview program are used to record the data. When the mechanism started the motion, data has been collected for 30 seconds.

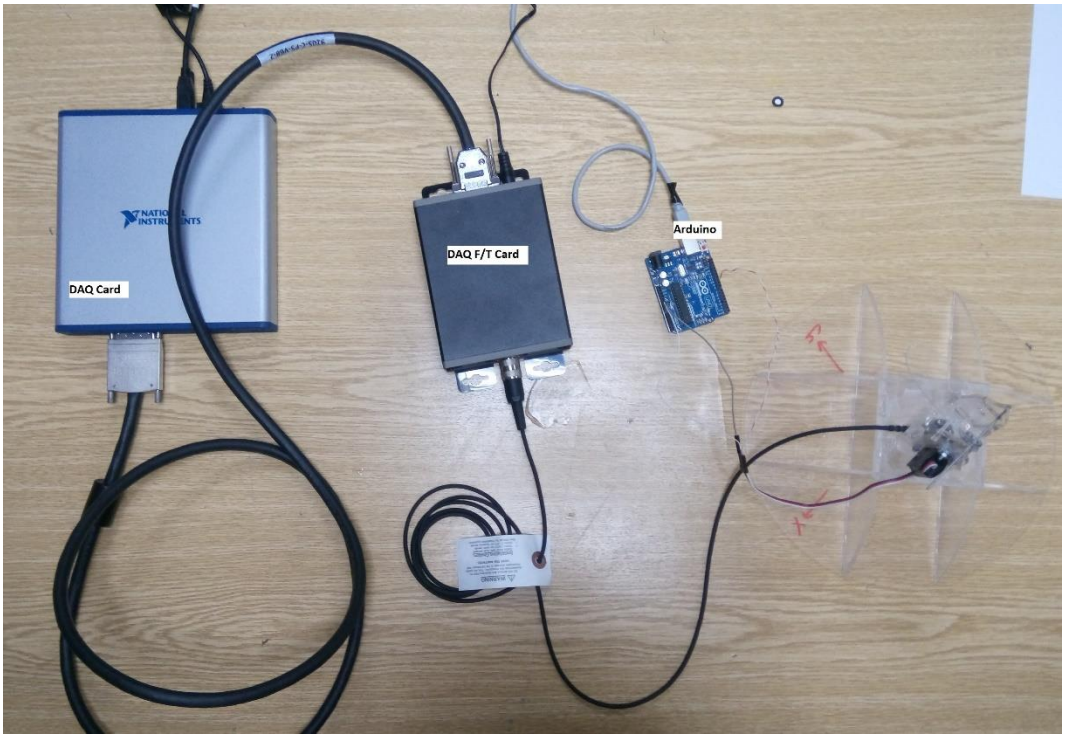

Figure 4. 5 Experimental setup

4.3.2 Force and Torque Sensor

Force and torque are measured by using 6-axis sensor ATI Nano17. The current force/torque sensor has very fine resolution of 3 mN of thrust and 16 μNm of moment. ATI Nano17 has sensing ranges ±12 N in x and y direction, and ±17 N in z direction (Table 4.3). It is made of stainless steel and it has a compact size with a 17 mm diameter and 14.5 mm height. Its weight is approximately 9 g [22]. Other setup components are Power Supply Box and DAQ card (Data Acquisition Board). ATI DAQ F/T card (Power Supply Box) (FTIFPS1) establishes connection between the sensor and National Instruments DAQ card. A National Instruments DAQ card with a 16 inputs, 16-bit multifunction (X1USB-6361) is transformed from analog signal to digital signals. Raw data are collected and recorded by using Labview program. At the beginning of the collection of data, calibration file is loaded. Bias can be disqualified by pressing the bias button. While collecting data, six-axis force and torque measurements are viewed at the same time. Output data can be saved by using the program (Figure 4.6).

Table 4. 3 ATI Nano 17 F/T specification [22]

Direction	Sensing ranges	Resolution
F_x	12 N	1/320 N
F_y	12 N	1/320 N
F_z	17 N	1/320 N
M_x	120 Nmm	1/64 Nmm
M_y	120 Nmm	1/64 Nmm
M_z	120 Nmm	1/64 Nmm
Calibration SI-12-0.12		

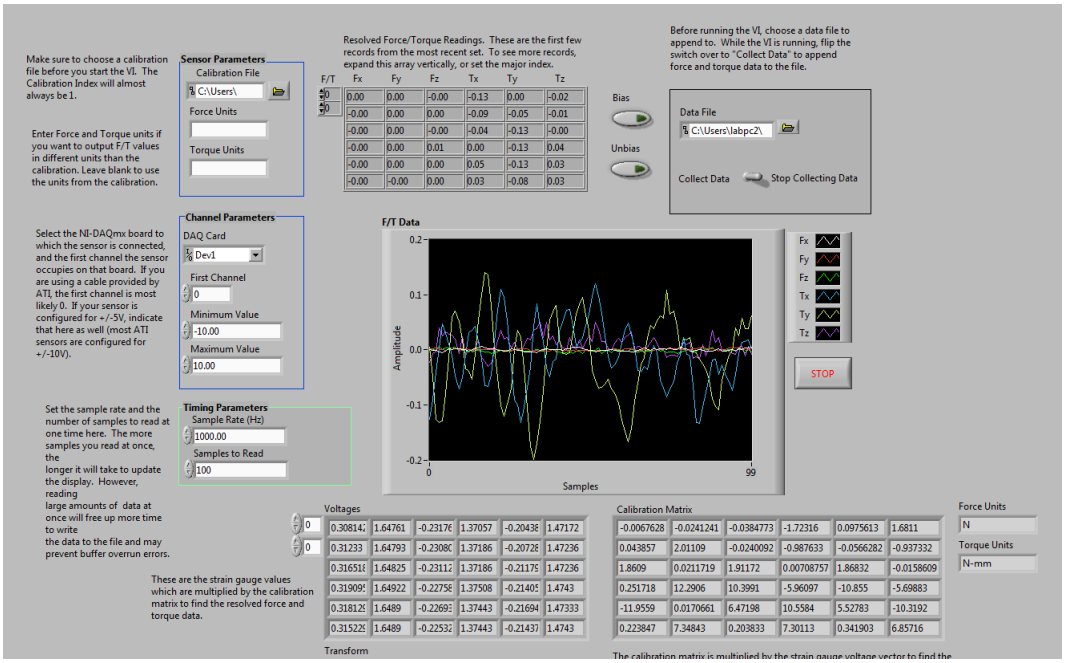

Figure 4. 6 Labview program interface

4.3.3 Labview Measurement Block

Throughout the experiments, collected data are come to Labview program in order to read. At the beginning of the collecting data, sensor parameter, channel parameter and timing parameter should be arranged. In the sensor parameter part, calibration file is loaded. In channel parameter part, NI-DAQ board and minimum-maximum voltage value are selected. In timing parameter part, suitable sample rate and samples to read are selected. Bias can be disqualified by pressing the bias button. While collecting data, three axis force and torque measurements are plotted at the same time (waveform graph). Calibration matrix and the voltages are shown. Output data can be saved by using the program (Figure 4.6).

Table 4. 4 The mass-mean force values

Dummy mass		**Program output [N]**
[g]	**[N]**	
0.2	0.0019	0.0025±0.0026
0.5	0.0049	0.0078±0.0029
1	0.009	0.0152±0.0024
2	0.0196	0.0312±0.0037
5	0.0490	0.0495±0.0026
10	0.0980	0.1102±0.0043
20	0.1961	0.1999±0.0028
50	0.4903	0.4724±0.0074
100	0.9806	1.0279±0.006

4.3.4 Force-Torque Sensor Measurement Verification

To verify the measurement of the sensor, the mass-force relationship of the sensor is examined. Dummy mass (0.2g, 0.5g, 1g, 2g, 5g, 10g, 20g, 50g, 100g) is placed on the sensor, and the program output is recorded for 30 second. The mean values and standard deviation of measurements are taken. In Figure 4.7, the mass-mean force relationship graph is shown and also in Table 4.4, the mass-mean force values are shown.

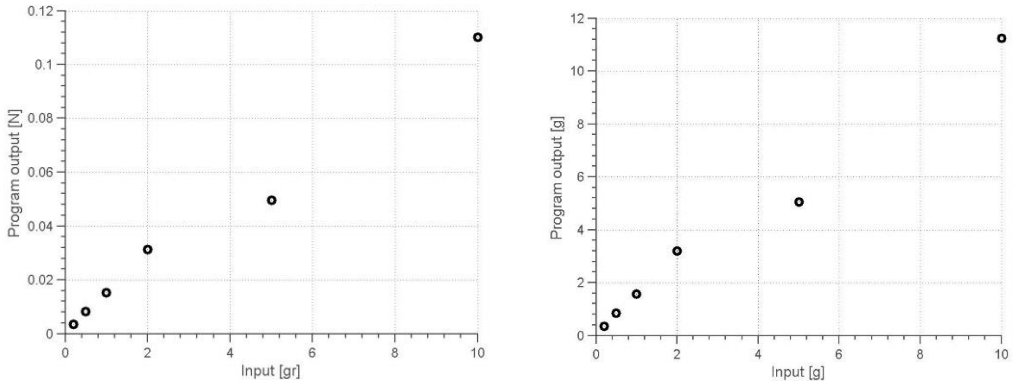

Figure 4. 7 Mass-mean force relationship

4.4 Experimental Procedure

Experimental procedure comprises mainly three parts: preparation, experiment and post-processing of data. Firstly, all electronic components and mechanism is connected each other. Then, all cable connections are checked before giving the electric in order to prevent short circuit. If mechanism is correct position, experiment can be started. Labview program is opened and gravitational effect set to zero by using bias button. After that, program is recorded the data for 30 seconds for all parts of experiment. In data post-processing, collected data is filtered to erase the noises. Finally, force and moment are plotted for each motion.

4.5 Experimental Uncertainty and Inertial Force

In general, all measurements have uncertainty. According to measurement verification, the force sensor does not have enough accuracy for very low force magnitudes like under 0.05 N. On the other hand, the sensor should be keep away any mechanical vibration during the experiment. Moreover, experimental results include electronic noise caused by the sensor equipment; and mechanical errors caused by bearings, segments, rods and servo gears. There are some manufacturing defects in mechanism especially rods which are connected between bearings and segments. Length of rod is a bit longer than usual. Therefore, there are little gaps between bearings and segments.

The net force which is measured by the F/T sensor is included gravity, added mass, inertial and aerodynamic forces. Gravity is reset by using bias button. Added mass is a virtual mass; it occurs especially in the fluid. For example, when a wing accelerates in a water, kinetic energy of water will be changed and become the acceleration reaction force. Therefore, added mass is insignificant for experiments in air. Viscous force in the fluid and pressure distribution around the wing produce to occur aerodynamic force. The inertial force is a force considers equal to mass and accelerating object or changing velocity of an object and it relates to Newton's Second Law (Eq. 4.1).

$$\overrightarrow{F} = m.\vec{a} \tag{4.1}$$

Stated in other words, inertial force is acting on the wing owing to the acceleration of flapping mechanism and wing related to exposed motion at the mechanism and wing root [24]. The wing generates aerodynamic forces but in the same time the inertial forces. Flapping mechanism generated only inertial force. Inertial force transcends the flight dynamics and also it transcends laminar flow regime of huge insects [30].

In this study, flapping mechanism frequency is 11.2 Hz with 41.5° flapping angle and 5.85 Hz with 85.9° flapping angle, hence acceleration of the wing is too big. In consequence, the inertial force should be removed the net force to find the net instantaneous aerodynamic force of the wing. In order to determine the inertial force,

two different methods are applied; numerical calculation and experimental analysis. In numerical calculation, angular velocity and angular acceleration are calculated by using instantaneous flapping angle as Ref [31]. The angular velocity is found by taking the first derivative of instantaneous flapping angle (Eq. 4.2) and then, the angular acceleration is found by taking the second derivative of instantaneous flapping angle (Eq. 4.3). In calculation, mass distribution establishes as uniform and the distance of the between the rotation axis and the wingtip is 83.47 mm which is called as R and also mass of the wing is taken 1.5 g.

$$w(t) = \frac{\partial \theta}{\partial t} \tag{4.2}$$

$$\alpha(t) = \frac{\partial w}{\partial t} \tag{4.3}$$

$$\overrightarrow{F} = -m.\vec{a} = -mr\vec{\alpha} \tag{4.4}$$

$$F = -\int_0^R \alpha r \rho dr = -\alpha \frac{r^2}{2} m = -\alpha \frac{R}{2} m \tag{4.5}$$

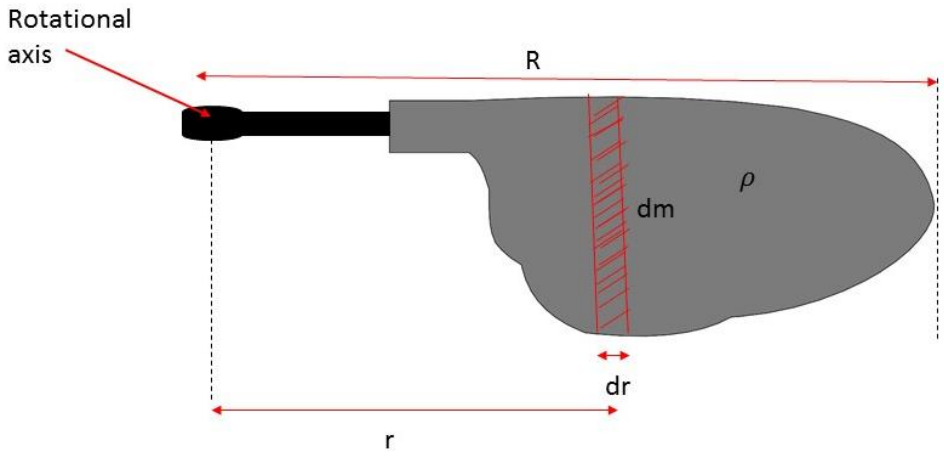

Figure 4.8 Schematic view of line element of thickness dr at a radius r

Table 4. 5 The calculated maximum angular velocity, acceleration and inertial force values for 2 cases

Case	Max Angular Velocity [rad/s]	Max Angular Acceleration [rad/s^2]	Max Inertial Force [N]
1	25.5010	1794.5	0.1123
2	27.5565	1012.9	0.0634

For the first case, the instantaneous flapping angle, angular velocity, angular acceleration and inertial force graphs are shown in Figure 4.9.

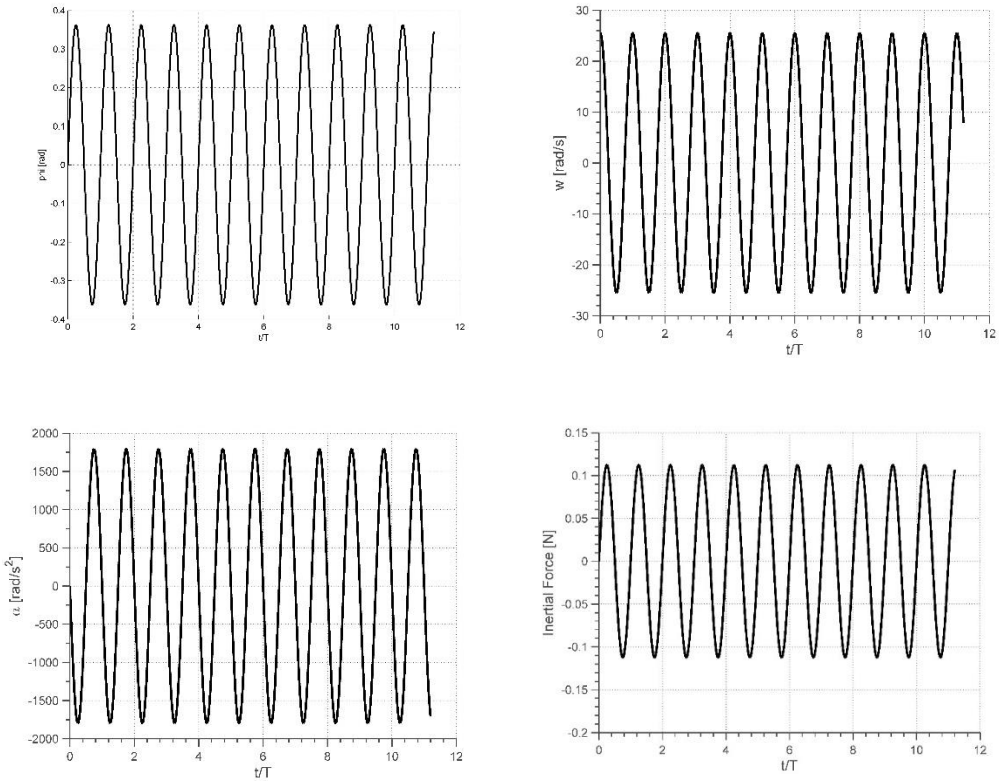

Figure 4. 9 The instantaneous flapping angle, angular velocity, angular acceleration and inertial force for case 1

Table 4.5 presents the calculated maximum angular velocity, acceleration and inertial force values for 2 cases. Angular velocity of case 1 is smaller than the ones of case 2; angular acceleration and inertial force of case 1 is higher than the ones of case 2 because case 1 has a higher frequency than case 2.

For first case, instantaneous flapping angle, angular velocity, angular acceleration and inertial force graphs are shown in Figure 4.10.

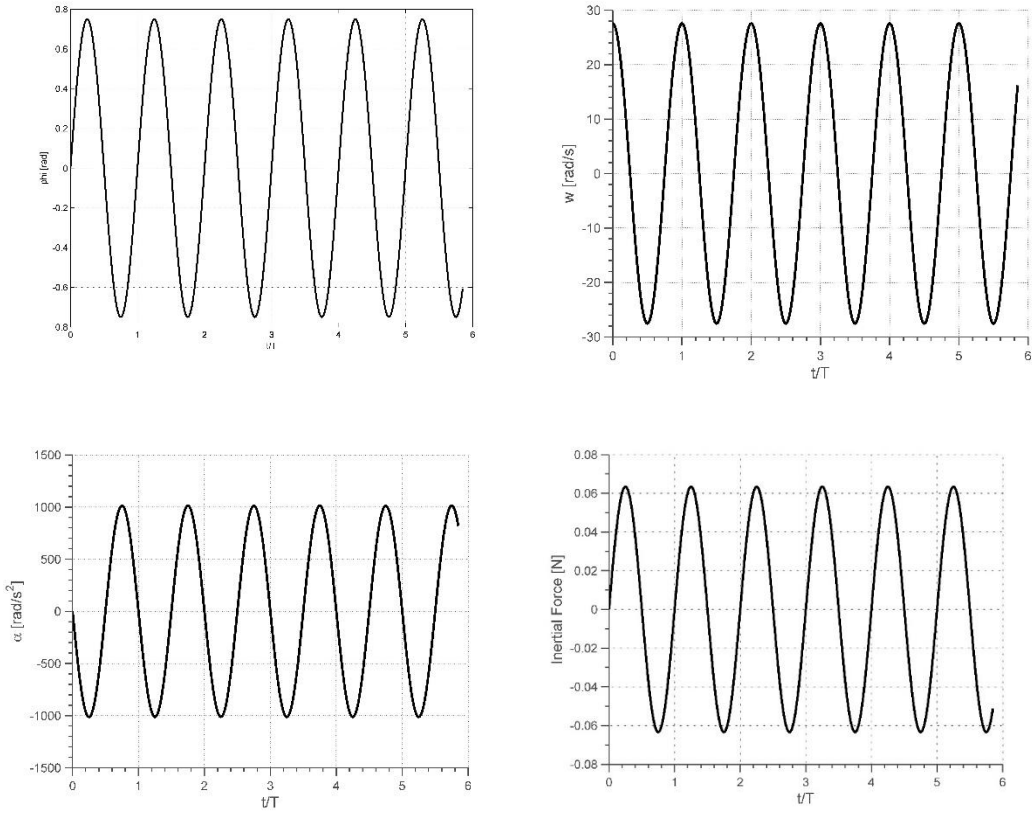

Figure 4. 10 The instantaneous flapping angle, angular velocity, angular acceleration and inertial force for case 2

The second method is experimental analysis, the wing having same features is manufactured and placed at the same distance from the center of rotation but different from other the wing, inertial model wing is assembled vertically (Figure 4.11). In this way, the wing having a same mass distribution and same shape is given only inertial force during the experiments. All cases are repeated with the inertial model wing.

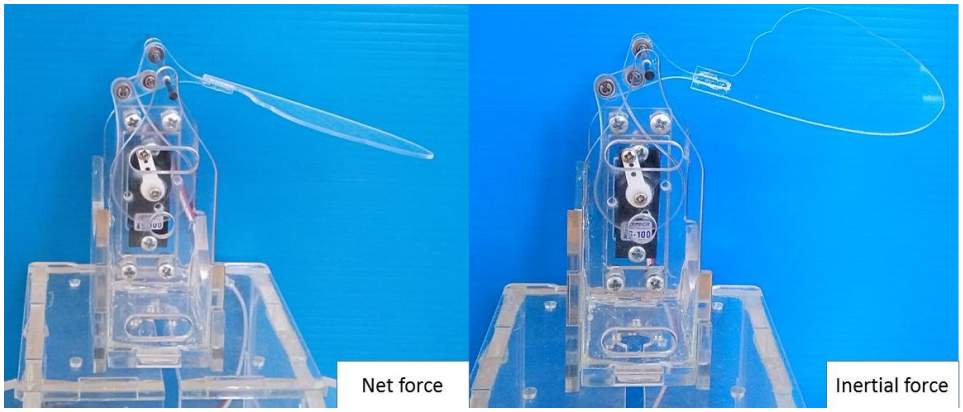

Figure 4. 11 The view of assembled wing for measurement net force and inertial force

4.6 Experimental Results

Experiments are done for all cases and all raw data are collected by using ATI Nano17 F/T sensor. Using raw data, Fast Fourier Transformation (FFT) is done. Motion frequency is at the highest force amplitude in the FFT analysis. In Figure 4.12, there are various force harmonics smaller than the first harmonic. The second largest pick is selected as a cut-off frequency value. For the 1st case, when flapping frequency is 11.2 Hz, the cut off frequency is 33.54 Hz. For the 2nd case, when flapping frequency is 5.85 Hz, the cut off frequency is 11.71 Hz. 5th order Butterworth low pass filter is used for separating data from noise. Table 4.6 indicates the parameters used for experimental cases.

Table 4. 6 Parameters of experimental cases

Case	Pitch	Input	Frequency	Flapping angle
1	0°	10°	11.2 Hz	41.5°
2	0°	20°	5.85 Hz	85.9°

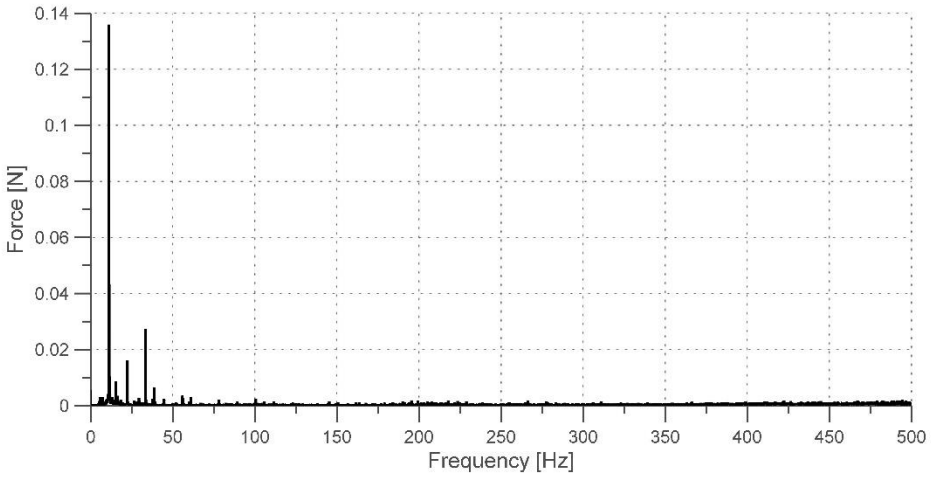

1st case

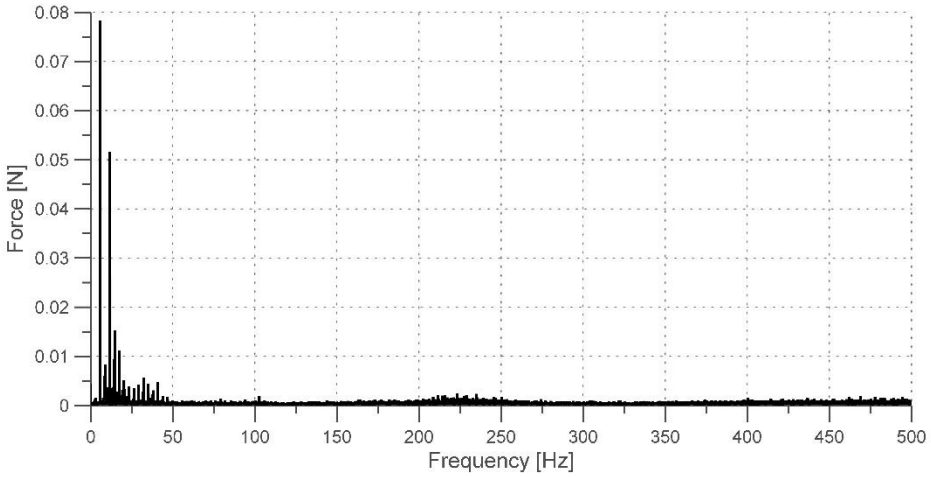

2nd case

Figure 4.12 FFT of z-direction (vertical) force for 2 cases

4.6.1 Case 1

For the 1st case, input angle is 10°, output angle is 41.5° at 11.2 Hz frequency. All data are recorded for 30 seconds. Figure 4.13 demonstrates the raw net force and raw inertial force time history for z-direction of sensor. Raw data means forces without applying any filter. The net force includes the aerodynamic force, inertial force, added

mass effect. As it can be seen in Figure 4.13, there are excessive fluctuations in the measurements. In order to eliminate these fluctuations, 5th order Butterworth Filter is used and frequencies higher than 33.54 Hz are deleted by filtering. Figure 4.14 shows raw and filtered net force time history for z-direction of the sensor.

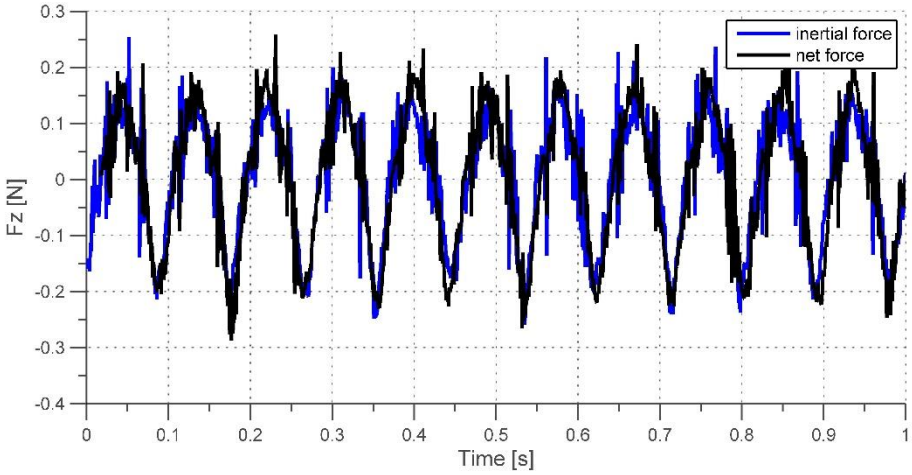

Figure 4.13 The raw net force and raw inertial force in the z-direction of the sensor for case 1

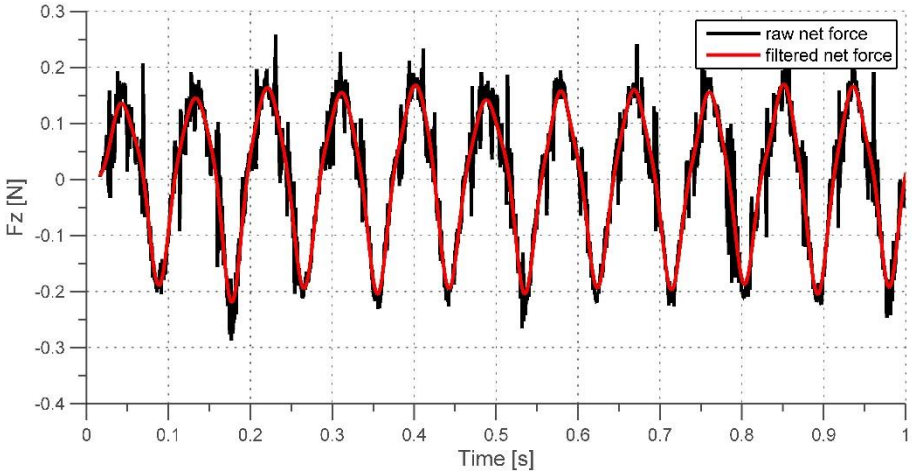

Figure 4.14 The raw and filtered net force in the z-direction of the sensor for case 1

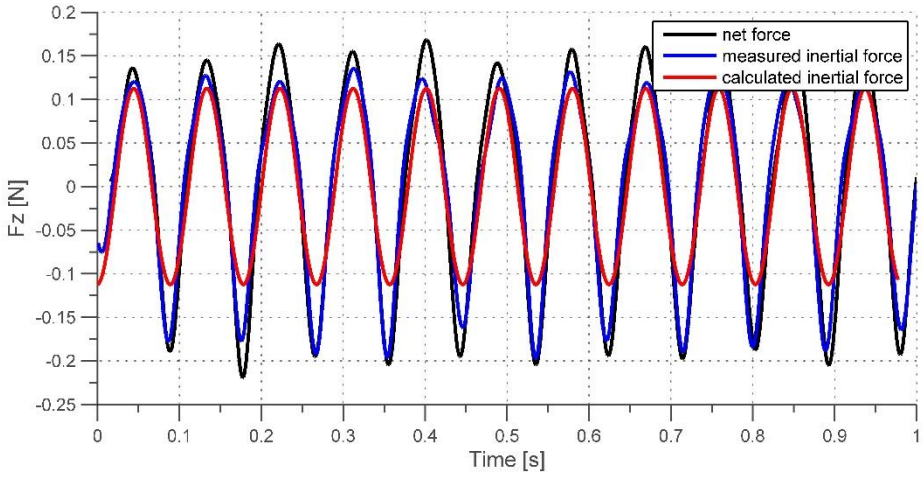

Figure 4.15 The filtered net and inertial force in the z-direction of the sensor for case 1

The net force and inertial force raw data are filtered with 33.54 Hz cut-off frequency. Figure 4.15 shows the variation in filtered net, filtered measured inertial force and calculated inertial for 1 second for z-direction of the sensor. The force are raged between 0.17 N and -0.21 N. In Figure 4.16, the results are estimated during the 58th period. Table 4.7 presents the maximum value of filtered net force is 0.1571 N at t*=58.36 whereas the minimum value of filtered net force is -0.2022 N at t*=58.85. At the same time, the maximum value of filtered inertial force is 0.1462 N while the minimum value of filtered inertial force is -0.1911 N. Difference between the net force and inertial force at these time gives aerodynamic force. At t*=58.36, difference between positive maximum values is 0.0109 N and difference between negative minimum values is 0.0111 N. Besides, calculated inertial force results approximate measured inertial force results. Moreover, lift force is calculated by using the numerical analysis (given in Chapter 5 in detailed). According to numerical analysis, the maximum lift force is 0.007847 N; on the other hand, the minimum lift force is -0.008143 N (Figure 4.17). There are some difference between experimental and numerical results. This difference may be stemmed from the sensor and mechanical imperfection.

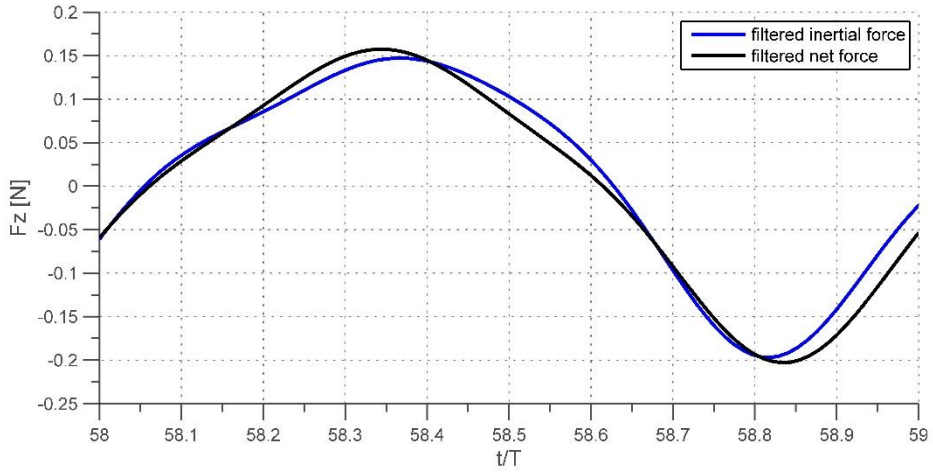

Figure 4.16 The filtered inertial force and net force for 58th period

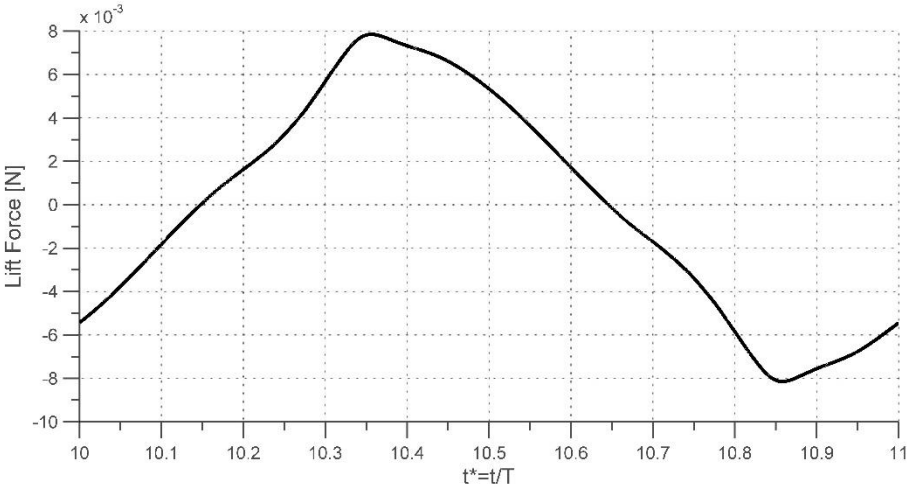

Figure 4.17 Lift calculated by using results of numerical analysis for 10th period

Figure 4.18 presents the variation in the raw data of net force for x-direction of the sensor. These values are very low and accuracy of the sensor is not enough. Hence, results of drag force cannot analysis, they looks like noise.

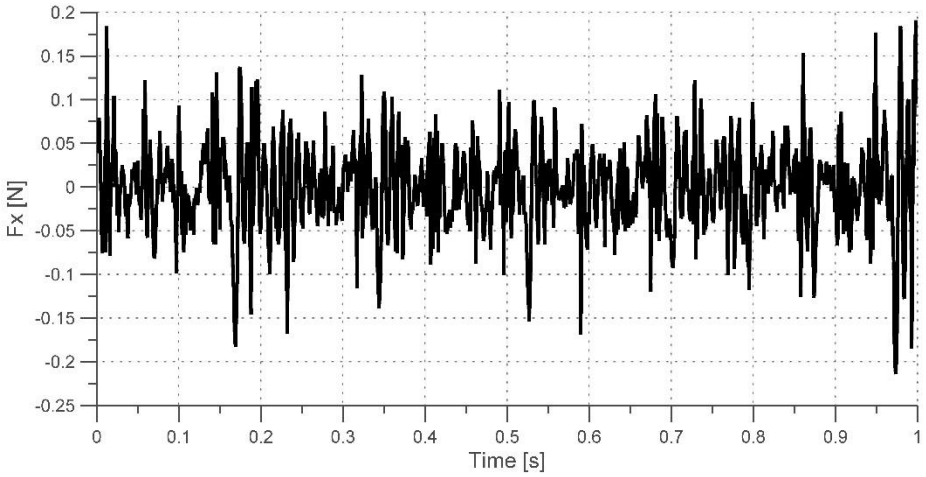

Figure 4.18 The raw data of net force in the x-direction of the sensor for case 1

Table 4.7 Comparative results of experimental case 1 and numerical case 1

	Measured Net Force		**Measured Inertial Force**		**Calculated Inertial Force**	**Measured Net-Measured Inertial**	**Numerical Analysis Results by CFD**	
	[N]	**t***	**[N]**	**t***	**[N]**	**[N]**	**[N]**	**t***
Max	0.157	58.3	0.1462	58.36	0.1123	0.0109	0.00784	10.36
Min	-0.20	58.8	-0.19	58.85	0.1123	-0.0111	-0.0081	10.86

4.6.2 Case 2

For the 2nd case, input angle is 20°, output angle is 85.9° at 5.85 Hz frequency. All data are recorded for 30 seconds. Figure 4.19 illustrates the variation in raw net force and raw inertial force time history for z-direction of the sensor. As it can be seen in Figure

4.19, there are excessive fluctuations in the measurements. In order to eliminate these fluctuations, 5th order Butterworth Filter is used and frequencies higher than 11.71 Hz are deleted by filtering. Figure 4.20 shows the variation in raw and filtered net force time history for z-direction of the sensor.

The net force and inertial force raw data are filtered with 11.71 Hz cut-off frequency. Figure 4.21 shows the variation in filtered net, filtered measured inertial force and calculated inertial for 1 second for z-direction of the sensor. The force are ranged between 0.095 N and -0.12 N. In figure 4.22, the results are presented during the 66th period. Table 4.8 shows the maximum value of filtered net force is 0.06582 N at t*=66.51 while the minimum value of filtered net force is -0.09783 N at t*=66.97. The maximum value of the filtered inertial force is 0.05055 N. The minimum value of the filtered inertial force is -0.07634 N. Difference between the net force and inertial force at these time gives aerodynamic force. At t*=66.51, difference between positive maximum value is 0.01527 N and difference between negative minimum value is 0.02149 N. Besides, calculated inertial force results approximate measured inertial force results. Moreover, lift force is calculated by using the numerical analysis (detailed in Chapter 5). According to numerical analysis, the maximum lift force is 0.005283 N; on the other hand, the minimum lift force is -0.005681 N (Figure 4.23). There are little difference between experimental and numerical results. This difference may be stemmed from the sensor and mechanical imperfection.

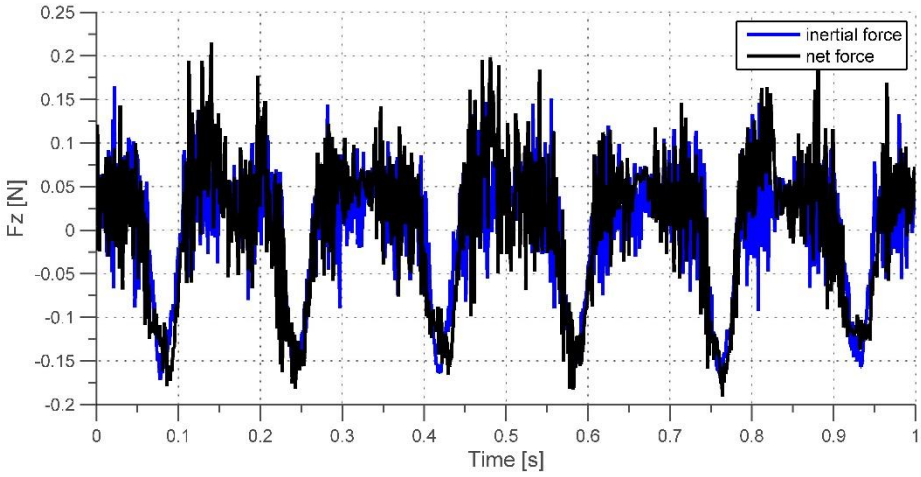

Figure 4.19 The raw net force and raw inertial force in the z-direction of the sensor for case 2

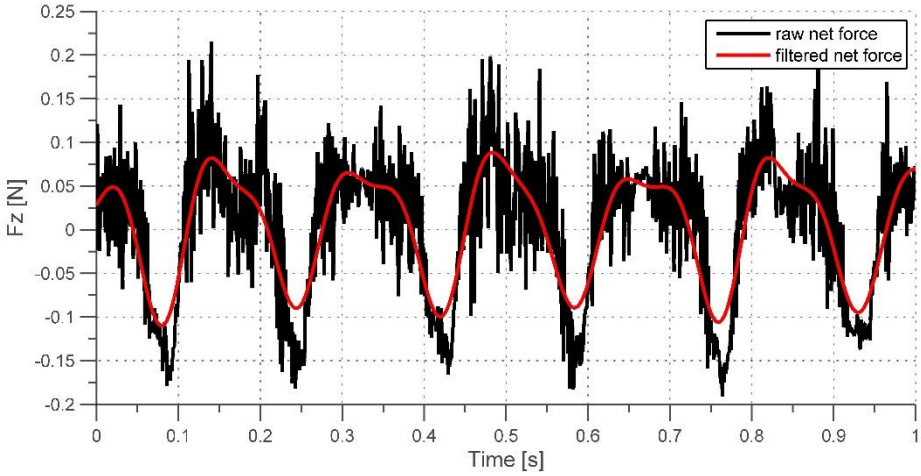

Figure 4.20 The raw and filtered net force in the z-direction of the sensor for case 2

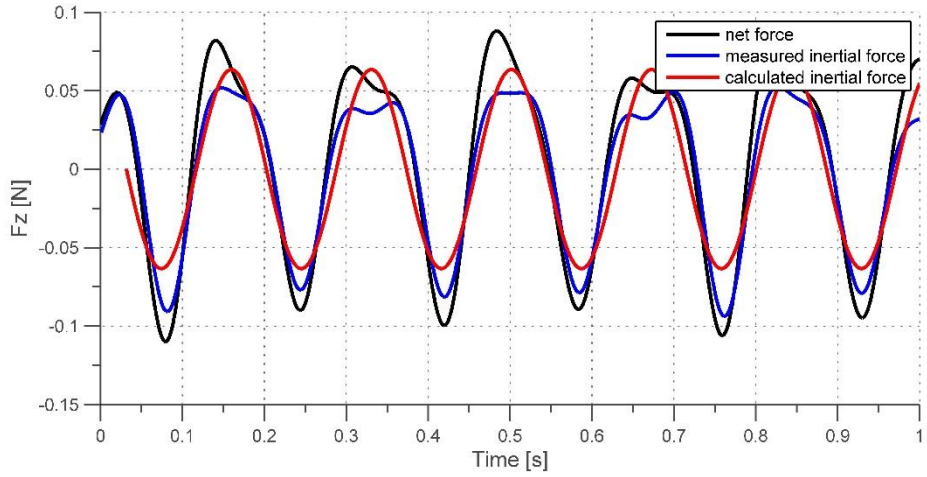

Figure 4.21 The filtered net and inertial force in the z-direction of the sensor for case 2

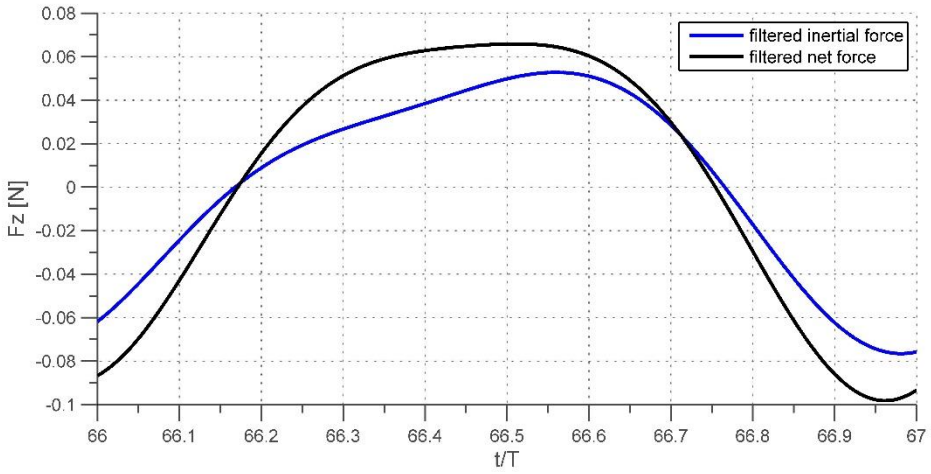

Figure 4.22 The filtered inertial force and net force for 66th period

Figure 4.24 demonstrates the variation in the raw data of net force for x-direction of the sensor. These values are very low and accuracy of the sensor is not enough. Hence, results of drag force cannot analysis, they looks like noise.

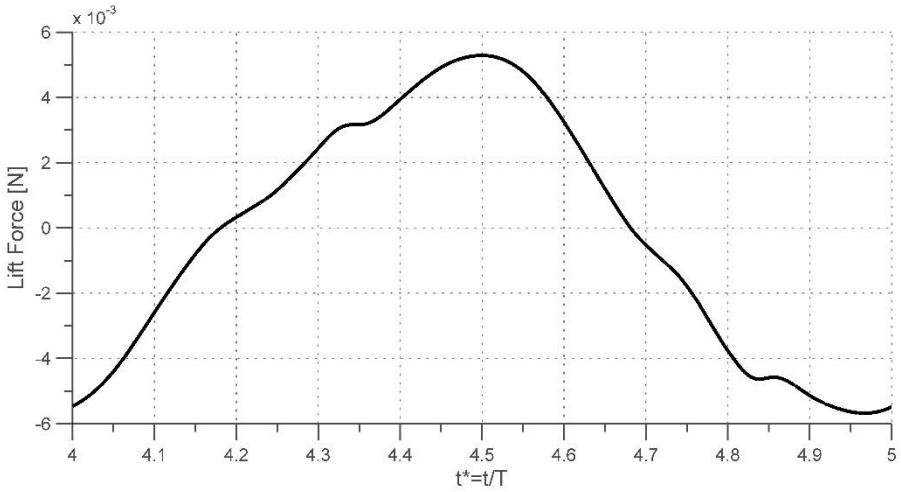

Figure 4.23 Lift calculated by using the results of numerical analysis for 4th period

Table 4. 8 Comparative results of experimental case 2 and numerical case 2

	Measured Net Force		**Measured Inertial Force**		**Calculated Inertial Force**	**Measured Net-Measured Inertial**	**Numerical analysis result by CFD**	
	[N]	**t***	**[N]**	**t***	**[N]**	**[N]**	**[N]**	**t***
Max	0.06582	66.51	0.0505	66.51	0.063	0.01527	0.0052	4.51
Min	-0.0978	66.97	-0.076	66.97	0.063	-0.02149	-0.005	4.97

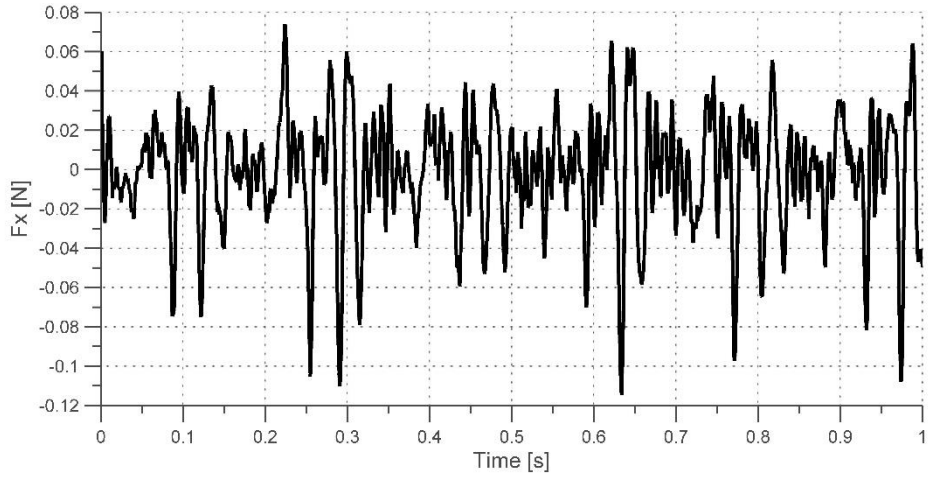

Figure 4. 24 The raw data net force in the x-direction of the sensor for case 2

4.7 Discussions for Experimental Analysis

The following points are considered after the analysis of the experimental simulations

- Measured inertial force and calculated inertial force is found approximately same.
- There are some errors and uncertainties caused by the mechanical imperfections.
- Experimental results reveal higher force magnitude than that of numerical results despite the removal of the inertial force. In these cases, wing deformation may be formed and may finally affected the results. The wing has a 1 mm thickness and is made of plexiglass. Although, plexiglass is a rigid material, wing deformation is caused bending moment and torsion.
- Mechanical uncertainties in case 2 are much more than the ones in case 1. As flapping angle in case 2 is higher than the one in case 1. Mechanical uncertainties in case 2 is higher than the one in case 1.
- In all force graphs, the deviations in the negative direction are observed. That is, absolute value of the peak in the positive direction is lower than the absolute value of the peak in the negative direction. The reason of this is higher flapping frequency, flexibility of the wing, gaps in mechanical parts: rods, segments and

bearings. In addition, that the flapping mechanism may require a higher angular acceleration for upstroke movement may cause that difference.

- As the flapping frequency increases the amplitude of the force increases. Case 1 has higher flapping frequency so has higher force amplitude.

CHAPTER 5

NUMERICAL ANALYSIS

In this section, numerical analysis of 3D wing model is done by Ansys-Fluent. The 3-D blow fly (Calliphora Erythocephala) wing is modelled 29.15 mm chord and 58.47 mm span having 1 mm thickness. The flapping motion is given to the wing model by user-defined function (UDF) using dynamic mesh option. The unstructured volume grids are suitable for moving the whole grid for hover mode with the wing model and deforming grid for forward flight with the wing model. In this study, Ansys-Fluent 14 is used to obtain all results [28].

5.1 Governing Equations

For hover and forward-flight conditions, governing equations are the incompressible flow, three-dimensional, the Navier-Stokes equations can be written as in equations 5.1. The inertial force terms are eliminated from the governing equations.

$$\frac{\partial u}{\partial x}+\frac{\partial v}{\partial y}+\frac{\partial w}{\partial z}=0 \tag{5.1a}$$

$$\rho\left(\frac{\partial u}{\partial t}+u\frac{\partial u}{\partial x}+v\frac{\partial u}{\partial y}+w\frac{\partial u}{\partial z}\right)=-\frac{\partial p}{\partial x}+\mu\left(\frac{\partial^2 u}{\partial x^2}+\frac{\partial^2 u}{\partial y^2}+\frac{\partial^2 u}{\partial z^2}\right) \tag{5.1b}$$

$$\rho\left(\frac{\partial v}{\partial t}+u\frac{\partial v}{\partial x}+v\frac{\partial v}{\partial y}+w\frac{\partial v}{\partial z}\right)=-\frac{\partial p}{\partial y}+\mu\left(\frac{\partial^2 v}{\partial x^2}+\frac{\partial^2 v}{\partial y^2}+\frac{\partial^2 v}{\partial z^2}\right) \tag{5.1c}$$

$$\rho\frac{\partial w}{\partial t}+u\frac{\partial w}{\partial x}+v\frac{\partial w}{\partial y}+w\frac{\partial w}{\partial z}\Big)=-\frac{\partial p}{\partial z}+\mu\left(\frac{\partial^2 w}{\partial x^2}+\frac{\partial^2 w}{\partial y^2}+\frac{\partial^2 w}{\partial z^2}\right) \tag{5.1d}$$

where x, y, z are the directions, u, v, w are the velocity components, t is the time, ρ is the density, p is the pressure and μ is kinematic viscosity [29].

5.2 Meshing and Solver

5.2.1 Meshing and Solver for Hover Mode

Ansys Meshing software is used for the unstructured volume grids. These types are suitable for moving the whole grid with the wing model because of hover mode. It is also possible to just move the wing by using remeshing options [32]. It should be noted that there is not any free stream velocity for hover mode.

The O-type far-field computational domain with radius of 1000 mm is used. Computational grid which comprises of tetrahedral cells is solved by the Navier-Stokes equations. The unstructured far-field mesh and the mesh distribution close to the wing mesh can be seen in Figure 5.1. Boundary condition for far-field domain is pressure-outlet; on the other hand, the wing surface is a wall. The flapping motion is given to the wing model by user-defined function (UDF) using dynamic mesh option. The UDF is written in the C programming language. Flapping motion (simple harmonic motion) which is performed along the sinusoidal wave applies with Eq. 3.7.

$$\phi(t) = \mathrm{A} * \sin(2\pi f t) \qquad (3.7)$$

The three dimensional, double precision pressure-based solver is selected. Least Squares Cell Based method is used for computing gradient and standard pressure interpolation is used. In this study laminar model is chosen as a flow model. Air density is 1.225 kg/m^3 and viscosity is 1.7894x10^{-5} kg/m-s. Smoothing methods is selected for grid adaption.

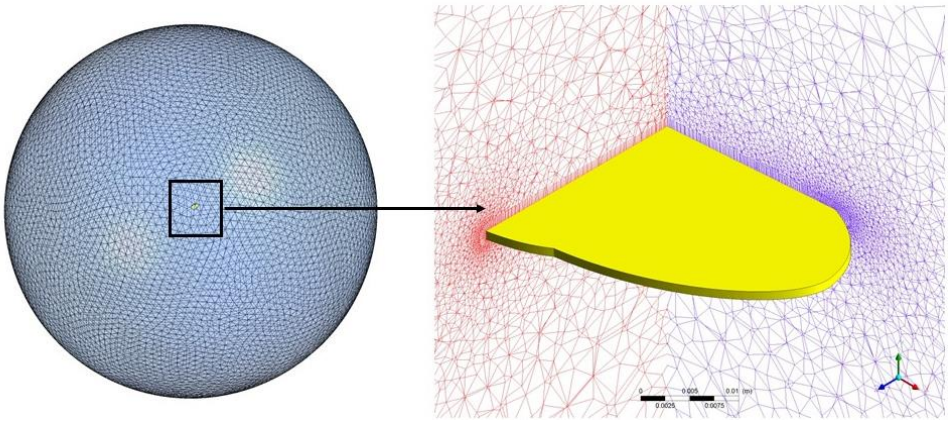

Figure 5. 1 Unstructured far-field mesh (left) and mesh close to the wing (right) for hover cases

Lift coefficient and drag coefficient values are calculated with Eqs. 5.2-5.3.

$$C_L = \frac{L}{\frac{1}{2}\rho U^2 S} \tag{5.2}$$

$$C_D = \frac{D}{\frac{1}{2}\rho U^2 S} \tag{5.3}$$

S is the area of the wing in Table 4.1. U is the velocity defined by the flapping frequency and the amplitude ($U=2\pi fA$). The velocity which is calculated by using angular velocity is 1.35 m/s for case 1 and the velocity is 1.5 m/s for case 2.

5.2.2 Meshing and Solver for Forward-Flight Mode

Gambit software is used for the unstructured volume grids. Different from hover mode, in forward flight mode, there is a free stream velocity. Inlet velocity is 3 m/s. Moving the whole grid with the wing model is not suitable for forward-flight mode. Therefore, in this case, smoothing and remeshing methods are selected for grid adaptation.

The H-type far-field computational domain with width-length-height of 2000 mm is used. The unstructured far-field mesh and the mesh distribution close to the wing mesh can be seen in Figure 5.2. Boundary condition for far-field domain is velocity-inlet and pressure-outlet; on the other hand, the wing surface is a wall.

Reynolds number values are calculated with Eq. 5.4.

$$Re = \frac{\rho U c}{\mu_{air}} \tag{5.4}$$

Reynolds number is approximately 6000. Therefore, laminar model is used.

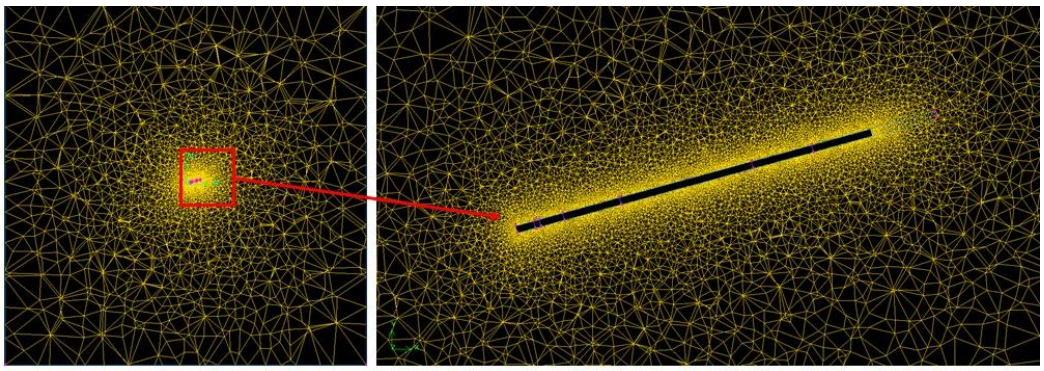

Figure 5.2 Unstructured far-field mesh (left) and mesh close to the wing (right) for forward-flight cases

5.3 Mesh Refinement Study

All computational mesh refinement simulations are performed on the rigid Calliphora Erythocephala wing model. Cases are performed by using three different O-type meshes in order to find the suitable mesh size. The course mesh, medium mesh and fine mesh are composed of 1084240 elements, 1967534 elements and 7329296 elements respectively (Table 5.1). In the mesh refinement study, same size of boundary layer is used. Simulation are done with a time step of $5x10^{-5}$s for case 1 and $1x10^{-4}$s. The graphs of lift coefficient are given during 10^{th} (case 1) and 4^{th} (case 2) periods. As it is shown in the Figure 5.3, lift coefficient results which are obtained from the coarse, medium and fine meshes are very similar. However, coarse mesh has some differences of close to the peaks by reason of insufficient number of nodes and elements. Therefore, the medium mesh is selected for the analysis of the current study.

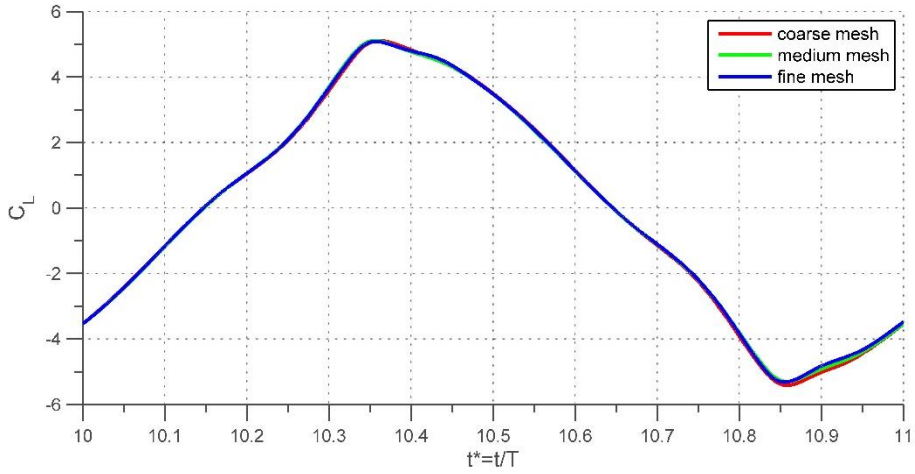

a)Lift coefficient for case 1

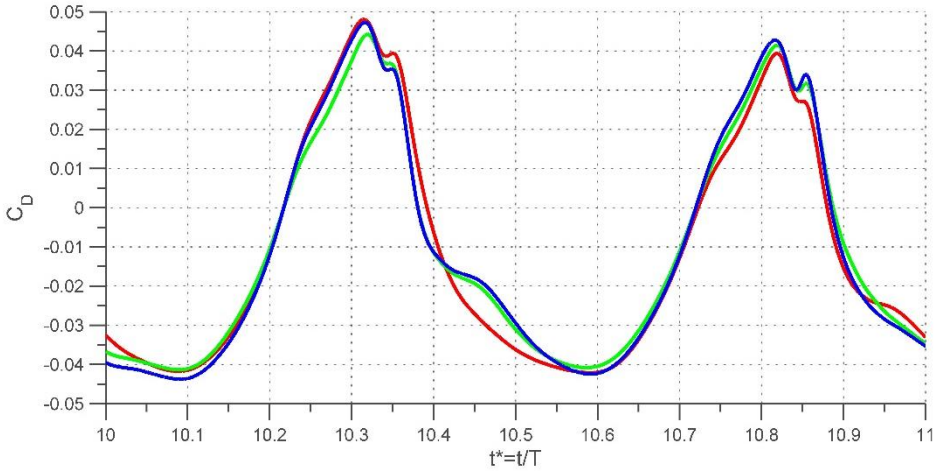

b)Drag coefficient for case 1

Figure 5. 3 Lift and drag coefficient during 10th period for mesh refinement study.

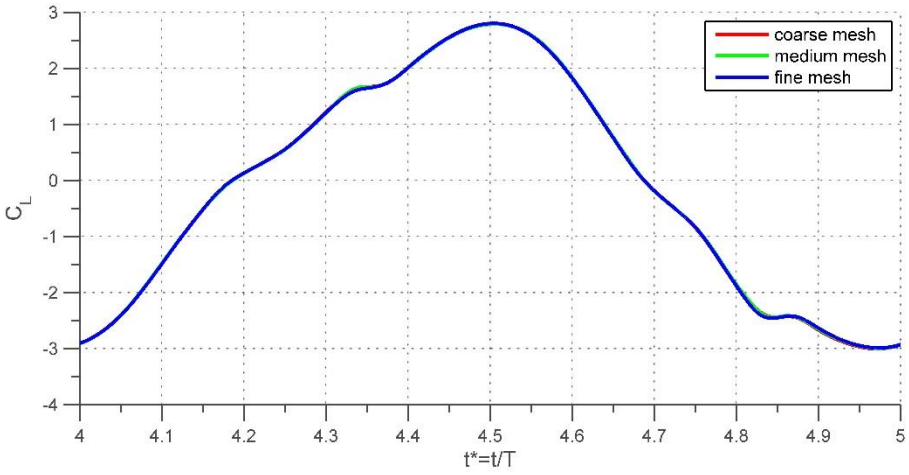

a)Lift coefficient for case 2

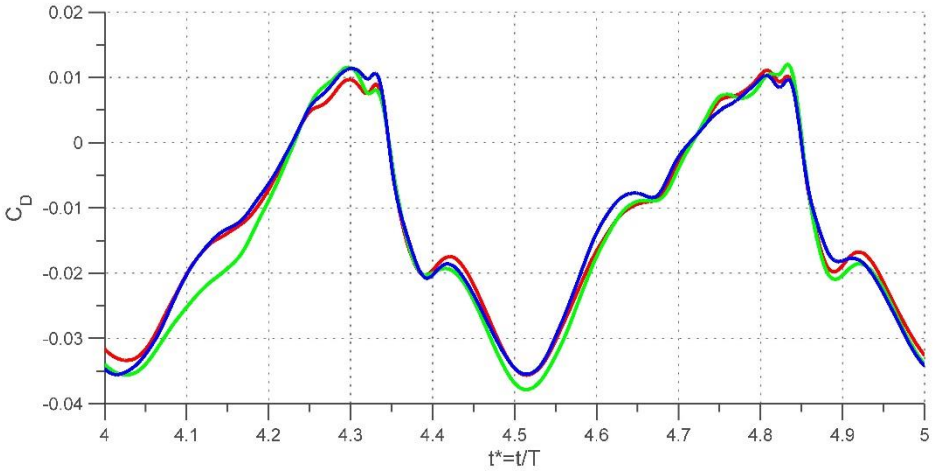

b)Drag coefficient for case 2

Figure 5. 4 Lift and coefficient during 4th period for mesh refinement study.

Table 5. 1 Node and element numbers for mesh refinement

	Node #	**Element #**
Coarse	260529	1084240
Medium	469195	1967534
Fine	1494527	7329296

5.4 Time Step Refinement Study

Time step refinement study is done for only case 2. Simulation are done with medium mesh and three different time step sizes such as $5x10^{-5}$s, $1x10^{-4}$s and $2x10^{-4}$s (Table 5.2). The graphs of lift coefficient during 4th (case 2) period are shown in Figure 5.3, lift coefficient results for the different time steps are very close to each other. Therefore, 1700 time-steps over one period of motion is selected for the current study.

Table 5. 2 Time step size

Δt [s]	$T/\Delta t$
$2x10^{-4}$	850
$1x10^{-4}$	1700
$5x10^{-5}$	3400

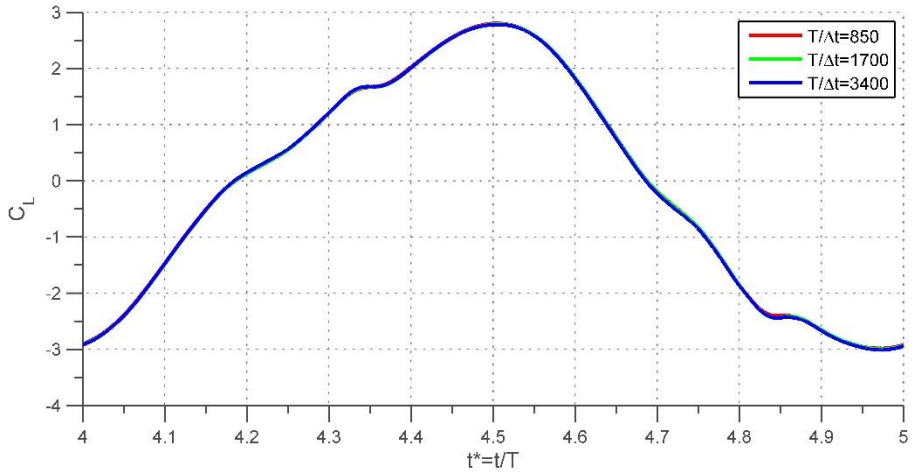

Figure 5. 5 Lift coefficient during 4th period for time refinement study (2nd case).

5.5 Numerical Results for Hover

5.5.1 Case 1

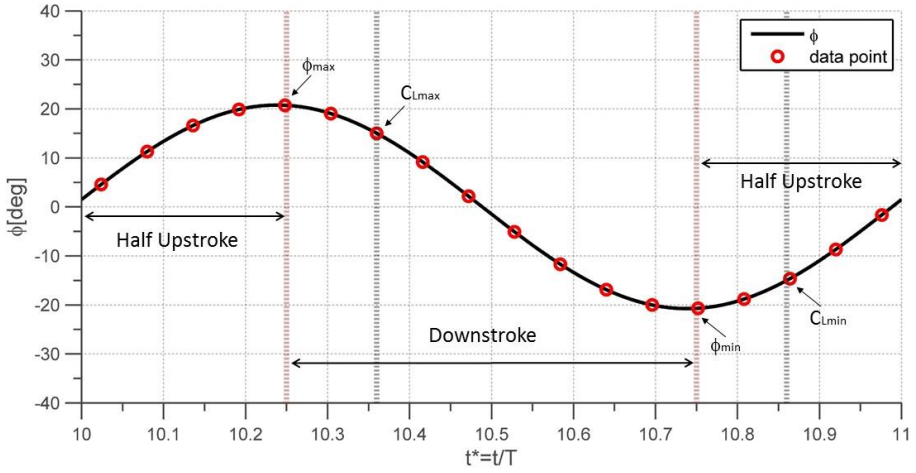

Figure 5. 6 Flapping angle for 10th period.

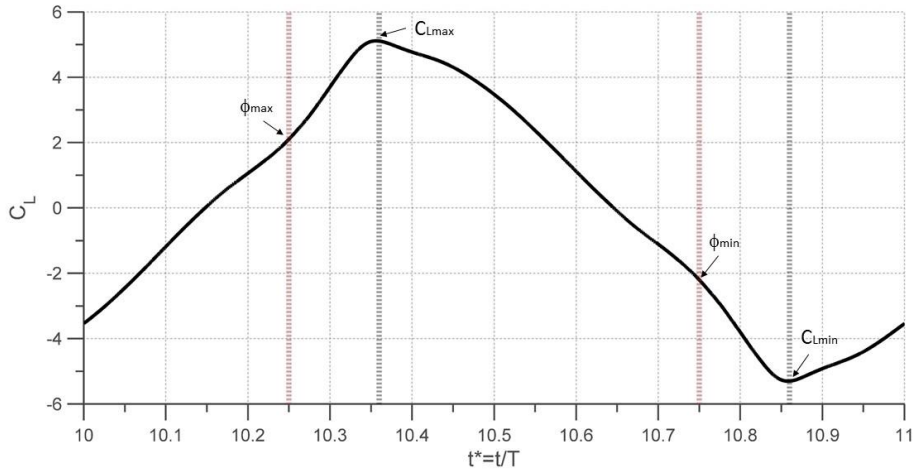

Figure 5. 7 Lift coefficient for 10th period.

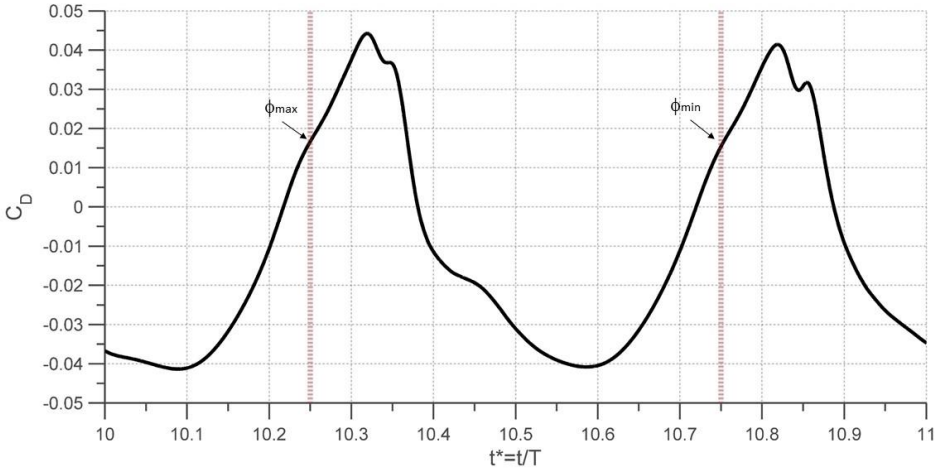

Figure 5. 8 Drag coefficient for 10th period.

The results of the 10th period are analyzed after the impulsive effects disappeared. Figure 5.6 shows the instantaneous flapping angle. Figure 5.7 and Figure 5.8 present the variation in lift coefficients and drag coefficients for the 10th period for 41.5° flapping angle at the 11.2 Hz flapping frequency. From Figure 5.6, it can be seen that absolute difference between C_{Lmax} and C_{Lmin} because during the downstroke the upward force is same with downward force during the upstroke. The maximum lift

coefficient position corresponds to ϕ= 15.01° at t*=10.36, which is below the maximum angular flapping angle ϕ= 20.75° at t*=10.25. The obtained maximum C_L value is 5.1. The minimum lift coefficient position corresponds to ϕ= -15.6° at t*=10.86, which is above the minimum angular flapping angle ϕ= -20.75° at t*=10.75. The obtained minimum C_L value is -5.3. The mean lift coefficient is -0.0492. Figure 5.8 illustrates that two different positive peak values are obtained in one period. One of them comprises during the donwstroke and the other one comprises during the upstroke. During the downstroke, the maximum drag coefficient is 0.04416 at t*=10.32 and the minimum drag coefficient is -0.04077at t*=10.58. On the other hand, during the upstroke, the maximum drag coefficient is 0.0414 at t*=10.82 and the minimum drag coefficient is -0.04136 at t*=10.09. The mean drag coefficient is -0.0103. Therefore, in this case, a very small thrust force is obtained.

Figure 5.9 shows the gauge static pressure distribution at the top and the bottom surface of the wing at ϕ_{max}, ϕ_{min}, C_{Lmax} and C_{Lmin} positions at 10^{th} period. The wing surface pressure contours are also plotted in the same figure at maximum deflection angles and at minimum and maximum lift coefficient positions. For ϕ_{max}, ϕ_{min}, C_{Lmax} and C_{Lmin} corresponding wing positions are highlighted in red color in Figure 5.8. When C_L is maximum a high pressure region is observed ($P-P_\infty$= +6 Pa) at a location close to the wing tip at the bottom surface. At the same time, at the upper surface of the wing, a suction region is be visualized ($P-P_\infty$= -6 Pa). On the other hand; when C_L is minimum, at the top of the wing, close to the wing tip a high over pressure region is observed.

Figure 5.10 presents that the 2D pressure distributions is observed ($P-P_\infty$= ±6 Pa) for 75% semi-span cross-section from the wing root at C_{Lmax} (left) (downstroke) and C_{Lmin} (right) (upstroke) positions at 10^{th} period. Leading edge vortices and trailing edge vortices are negative.

Figure 5.11 shows the position of root, tip of the wing, leading edge and trailing edge. This view is the same view given in Figure 5.10 and Figure 5.15 for different time instances. Leading edge vortex is smaller than trailing edge vortex.

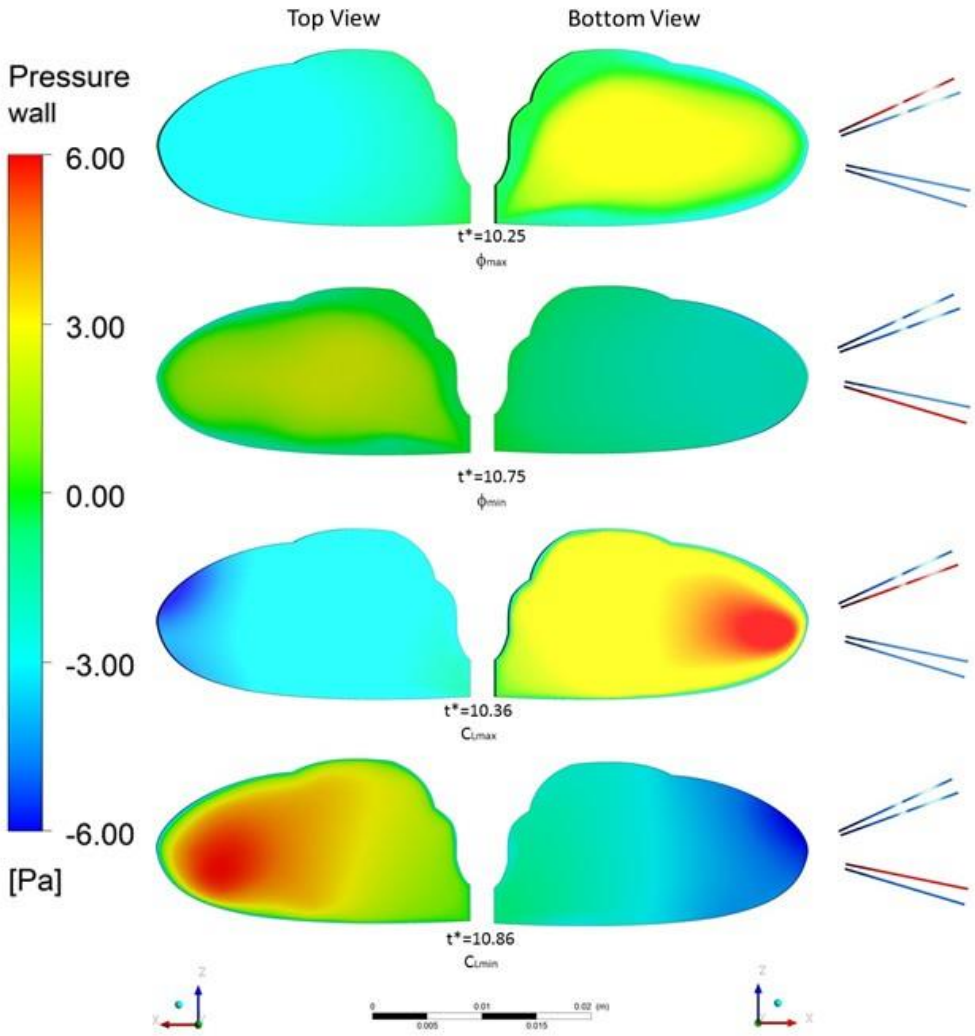

Figure 5. 9 Gauge static pressure (P-P$_\infty$) at the top and the bottom surfaces of the wing at ϕ_{max}, ϕ_{min}, C_{Lmax} and C_{Lmin} positions at 10th period (case 1).

Figure 5.12 shows the x-vorticity (left) and the z-vorticity (right) distribution for one period. Blue regions indicate positive vorticity (CCW) and red regions indicate negative vorticity (CW). In the x-vorticity distribution, during the downstroke the positive vorticity side displaced from trailing edge to the leading edge; on the other hand, during the upstroke the positive vorticity side displaced from leading edge to the trailing edge. The majority of the vorticity develops at the bottom surface of the wing at the mid-upstroke (t*=10); on the other hand, the majority of the vorticity develops at the upper surface of the wing at the mid-downstroke (t*=10.5). In the z-vorticity distribution, positive vorticity is bound to the wing's upper surface during mid-upstroke and during mid-downstroke. The positive vorticity side is displaced from the

root to the tip when the flap direction changes. In both cases, majority of the vorticity occurs at the wing tip and towards to the wing tip vorticities separate from the wing. Consequently, vortex at the root is smaller than the vortex at the tip.

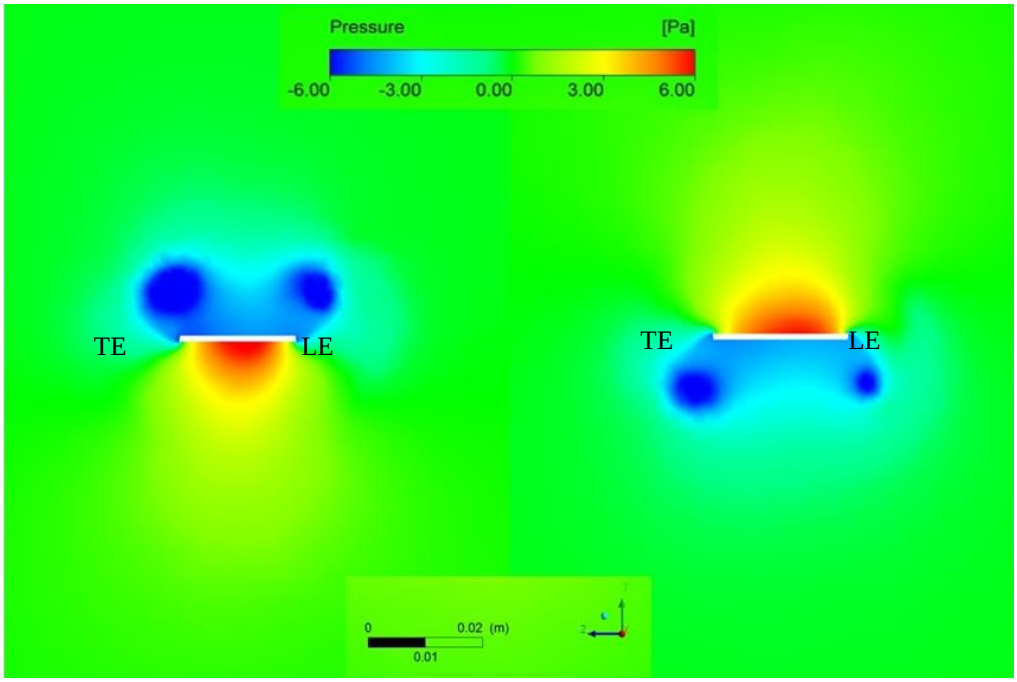

Figure 5.10 2D Pressure distributions for 75% semi-span cross-section from the wing root at C_{Lmax} (left) and C_{Lmin} (right) positions at 10^{th} period (case 1)

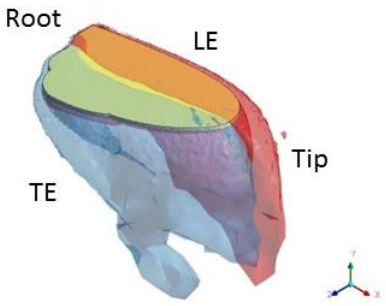

Figure 5. 11 Wing isometric view

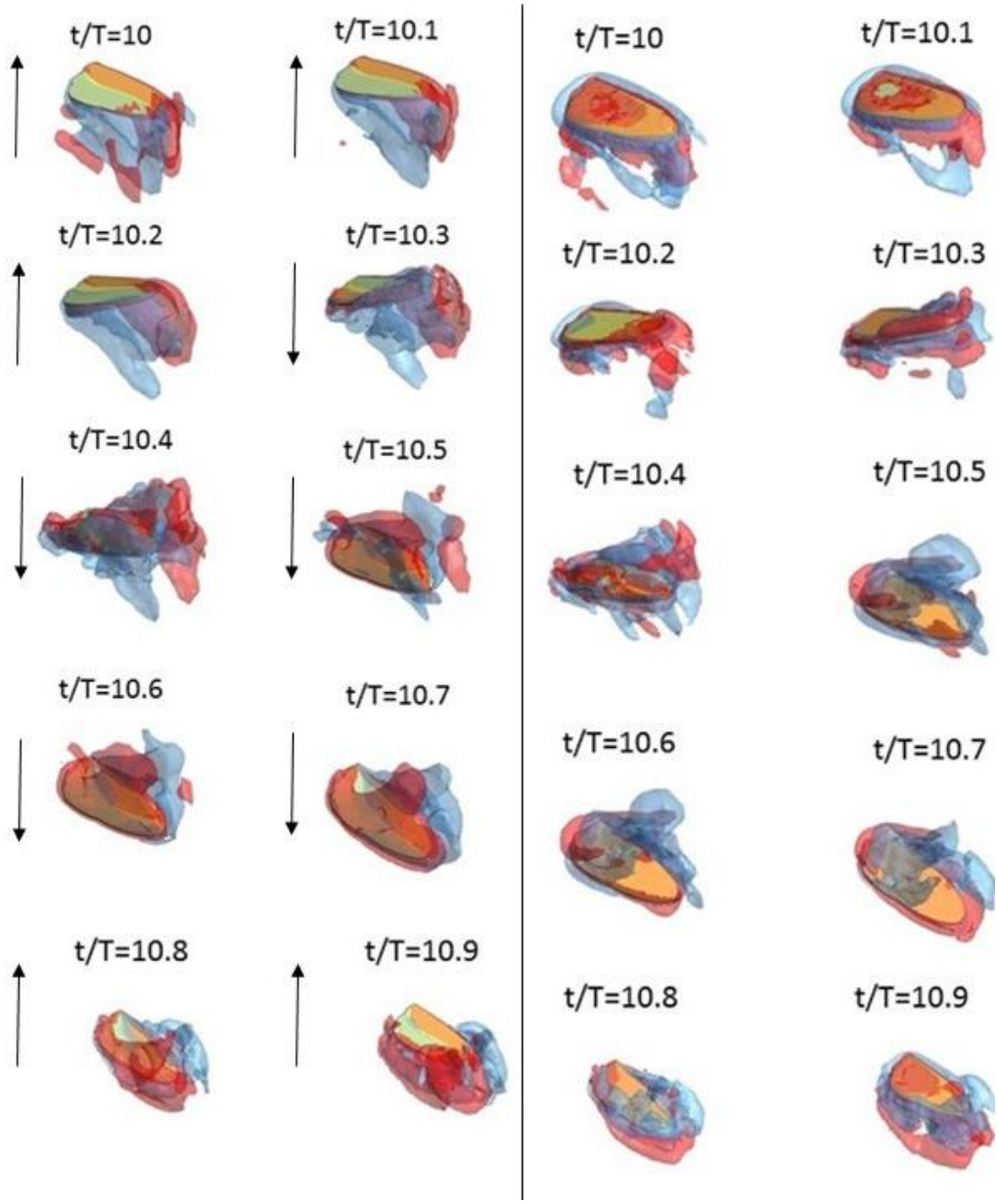

Figure 5. 12 Iso-surfaces of x-vorticity (left) and z-vorticity (right) at different time instances during 10^{th} period (case 1)

5.5.2 Case2

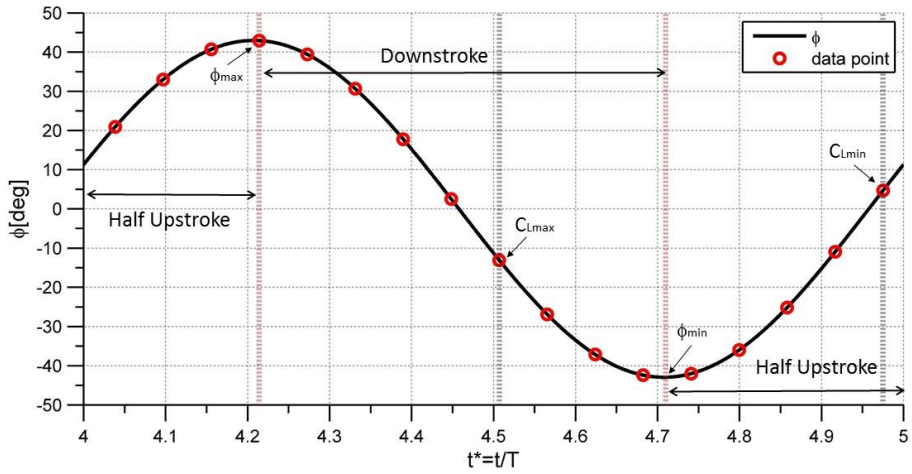

Figure 5. 13 Flapping angle for 4th period.

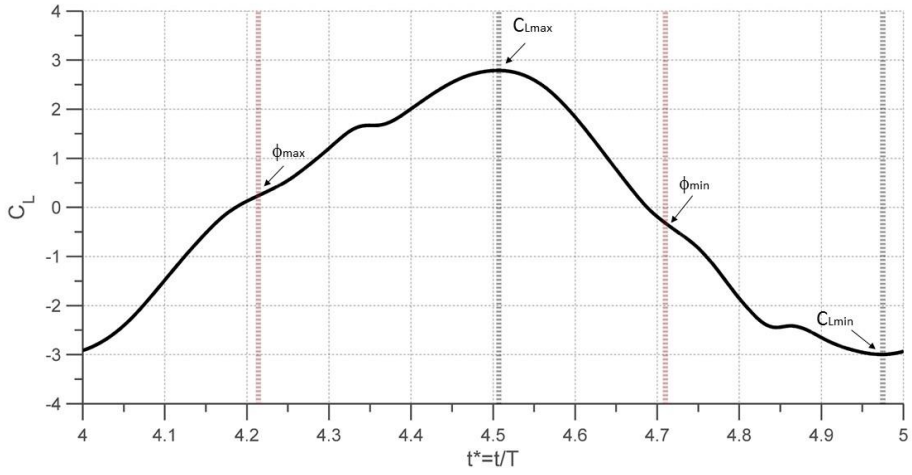

Figure 5. 14 Lift coefficient for 4th period.

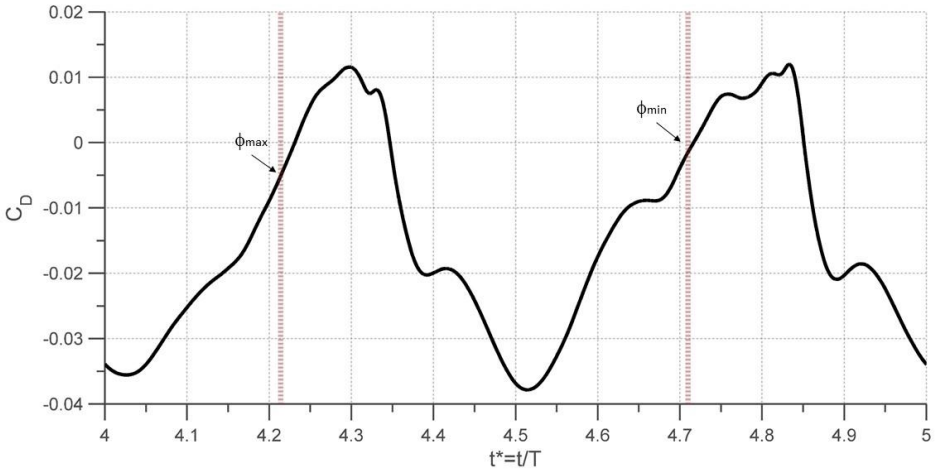

Figure 5. 15 Drag coefficient for 4th period.

The results are investigated during the 4th period after the impulsive effects disappeared. Figure 5.13 shows the instantaneous flapping angle. Figure 5.14 and Figure 5.15 illustrate the variation in lift coefficient and drag coefficient for 4th period for 85.9° flapping angle at the 5.85 Hz flapping frequency. Figure 5.14 shows range of lift coefficient is approximately zero because during the downstroke the upward force is as same as downward force during the upstroke. The maximum lift coefficient position corresponds to ϕ=-13.08° at t*=4.51, which is below the maximum angular flapping angle ϕ= 42.95° at t*=4.21. The obtained maximum C_L value is 2.79. The minimum lift coefficient position corresponds to ϕ= 4.71° at t*=4.975, which is above the minimum angular flapping angle ϕ= -42.95° at t*=4.7. The obtained minimum C_L value is -2.99. The mean lift coefficient is -0.11. Figure 5.15, it can be seen that, the wing produces thrust (negative drag) during the one period. Figure 5.15 illustrates that two different positive peak values are obtained in one period. One of them comprises during the donwstroke and the other one comprises during the upstroke. During the downstroke, the maximum drag coefficient is 0.01152 at t*=4.296 and the minimum drag coefficient is -0.03785 at t*=4.514. On the other hand, during the upstroke, the maximum drag coefficient is 0.01196 at t*=4.833 and the minimum drag coefficient is -0.03556 at t*=4.025. The magnitude of the peak in the downstroke is smaller than the magnitude of the peak in the upstroke. The mean drag coefficient is -0.014.

Difference between the maximum and minimum drag coefficient is negative. Therefore, in case 2, propulsive thrust (negative drag) force is obtained in the chordwise direction.

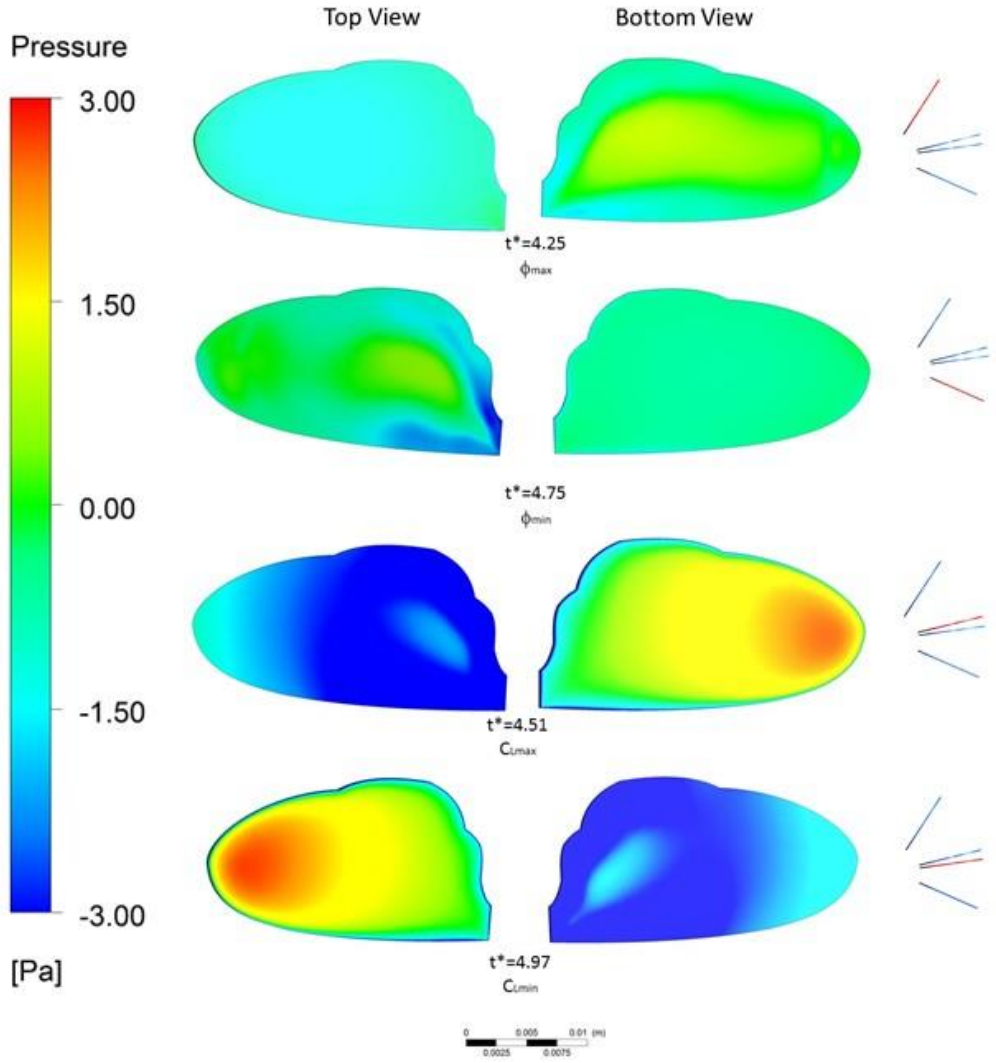

Figure 5. 16 Gauge static pressure (P-P$_\infty$) at the top and the bottom surfaces of the wing at ϕ_{max}, ϕ_{min}, C_{Lmax} and C_{Lmin} positions at 4th period (case 2).

Figure 5.16 shows gauge static pressure distribution at the top and the bottom surfaces of the wing at ϕ_{max}, ϕ_{min}, C_{Lmax} and C_{Lmin} positions at 4th period. The wing surface pressure contours are also plotted in the same figure at maximum deflection angles

and at minimum and maximum lift coefficient positions. For ϕ_{max}, ϕ_{min}, C_{Lmax} and C_{Lmin} corresponding wing positions are highlighted in red color in Figure 5.16. When C_L is maximum, at the bottom surface of the wing, close to the wing tip a high over pressure region is observed ($P-P_\infty$= +3 Pa), in the meantime, at the upper surface of the wing, a suction region can be visualized ($P-P_\infty$= -3 Pa). On the other hand; when C_L is minimum, at the top of the wing, close to the wing tip a high over pressure region is observed.

Figure 5.17 shows the 2D pressure distributions is observed ($P-P_\infty$= ±3 Pa) for 75% semi span cross section from the wing root at C_{Lmax} (left) (downstroke) and C_{Lmin} (right) (upstroke) positions at 4^{th} period. Leading edge vortices and trailing edge vortices are negative. Leading edge vortex is bigger than trailing edge vortex.

Figure 5.18 shows the x-vorticity (left) and the z-vorticity (right) distribution for one period. Blue regions indicate positive vorticity (CCW) and red regions indicate negative vorticity (CW). In the x-vorticity distribution, during the downstroke the positive vorticity side displaced from trailing edge to the leading edge; on the other hand, during the upstroke the positive vorticity side displaced from leading edge to the trailing edge. The majority of the vorticity improves on the bottom surface of the wing at the mid-upstroke (t*=4); on the other hand, the majority of the vorticity improves on the upper surface of the wing at the mid-downstroke (t*=4.5). In the z-vorticity distribution, positive vorticity is bound to the wing's upper surface during mid-upstroke and during mid-downstroke, the positive pressure side displaced from the root to the tip when the flap direction changes. In both cases, majority of the vorticity has occurred at the wing tip and towards to the wing tip vorticities separate from the wing. Tip vortices have an important role in hover cases. Consequently, vortex at the root is smaller than the vortex at the tip.

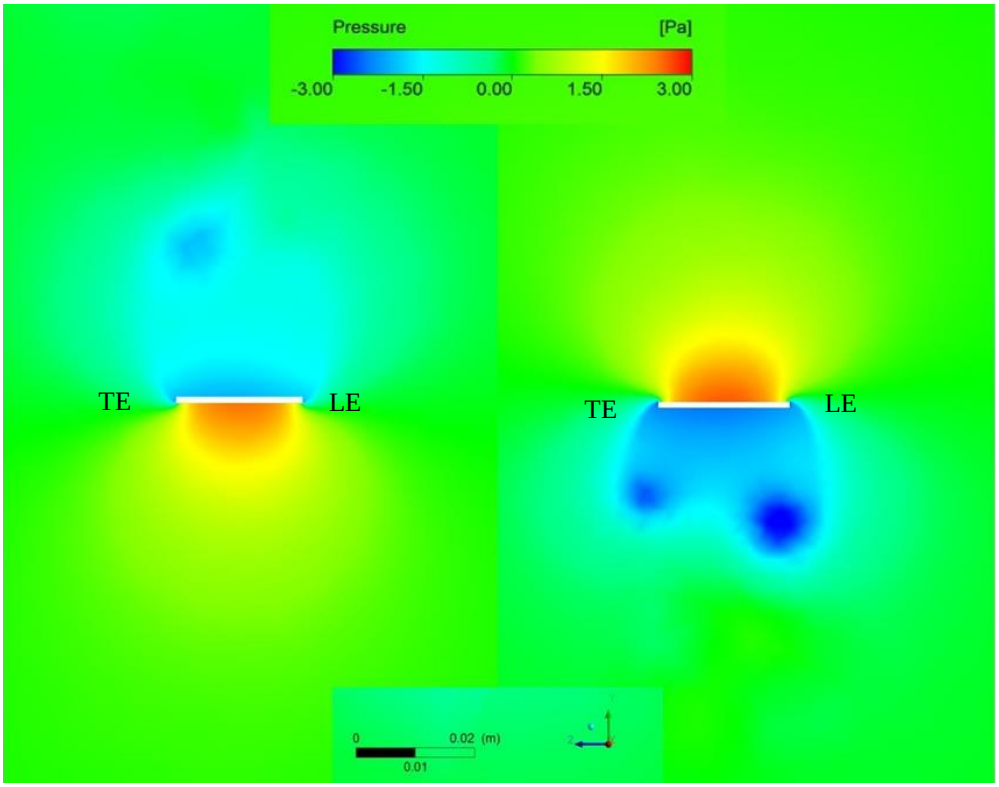

Figure 5.17 2D Pressure distributions for 75% semi-span cross-section from the wing root at C_{Lmax} (left) and C_{Lmin} (right) positions at 4^{th} period (case 2).

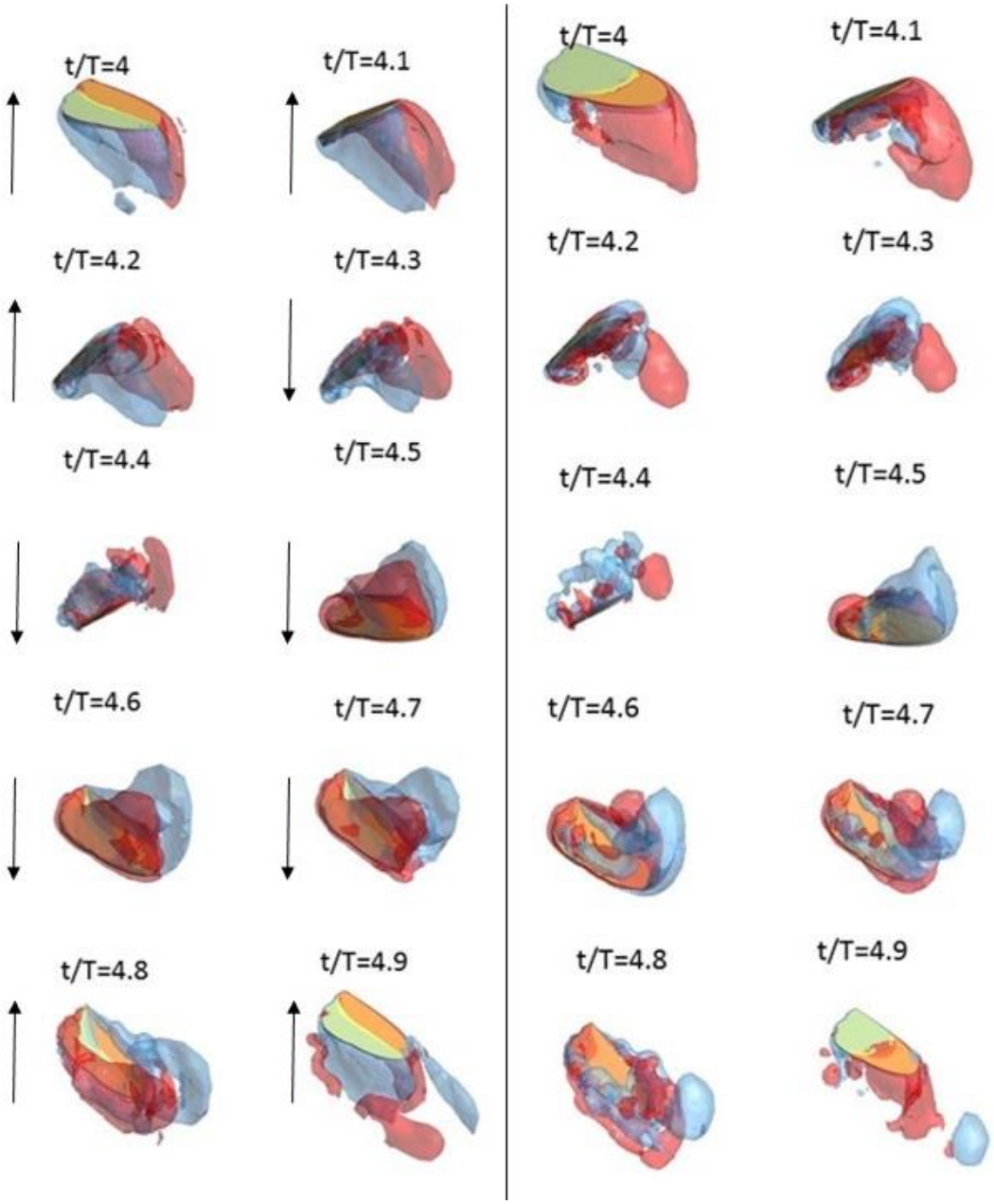

Figure 5. 18 Iso-surfaces of x-vorticity (left) and z-vorticity (right) at different time instances during 4th period (case 2)

5.6 Numerical Case 2 for Forward-Flight

In case 2 for forward-flight, flapping angle is 85.9° at 11.2 Hz flapping frequency. The inlet velocity is 3m/s.

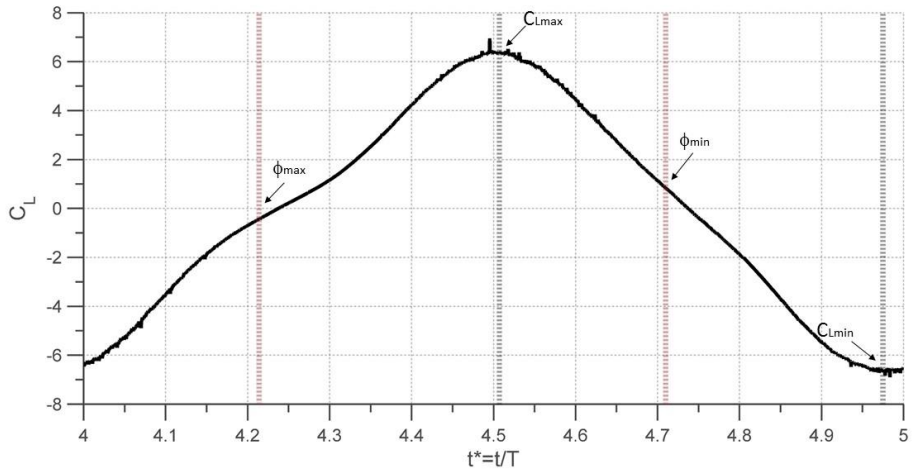

Figure 5. 19 Lift coefficient for 4th period

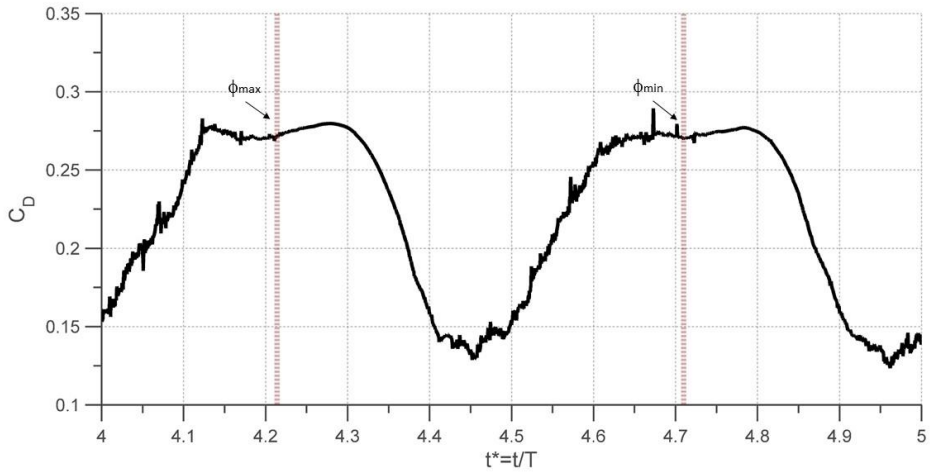

Figure 5. 20 Drag coefficient for 4th period.

The results are analyzed during the 4th period in forward-flight case. Figure 5.19 and Figure 5.20 present the variation in lift coefficient and drag coefficient for 4th period

for 85.9° flapping angle at the 5.85 Hz flapping frequency. Figure 5.19 it can be seen that absolute difference between C_{Lmax} and C_{Lmin} because during the downstroke the upward force is same with downward force during the upstroke. The obtained maximum C_L value is 6.44. The obtained minimum C_L value is -6.6. The mean lift coefficient is -0.0704. Lift coefficient at forward-flight case is twice as big as lift coefficient at hover case. Figure 5.20, it can be seen that, range of the value is positive, therefore, the wing produces drag. In Figure 5.20, two peaks develop during one period. One of them starts to develop at the end of the upstroke and go on at the beginning of the downstroke. The other one starts to develop at the end of the downstroke and go on at the beginning of the upstroke. The mean drag coefficient is 0.2228. That is, different from the hover case, in forward-flight case, positive drag force is obtained in the chordwise direction.

Figure 5.21 shows gauge static pressure distribution at the top and bottom surface of the wing at ϕ_{max}, ϕ_{min}, C_{Lmax} and C_{Lmin} positions at 4^{th} period for forward-flight. Wing surface pressure contours are also plotted in the same figure at maximum deflection angles and at minimum and maximum lift coefficient positions. For ϕ_{max}, ϕ_{min}, C_{Lmax} and C_{Lmin} corresponding wing positions are highlighted in red color in Figure 5.21. When C_L is maximum, at the bottom surface of the wing, along the leading edge and close to the wing tip a high over pressure region is observed ($P-P_\infty$= +3 Pa), in the meantime, at the upper surface of the wing, a suction region can be visualized ($P-P_\infty$= -3 Pa). On the other hand; when C_L is minimum, at the top of the wing, close to along the leading edge and close to the wing tip a high over pressure region is observed. The leading edge vortices occur a low pressure area in the upper side of the wing which is the suction side of the wing at C_{Lmax} position; on the other hand, the leading edge vortices occur a high pressure area in the bottom side of the wing. Magnitude of the gauge static pressure at forward-flight case is larger than pressure at hover case.

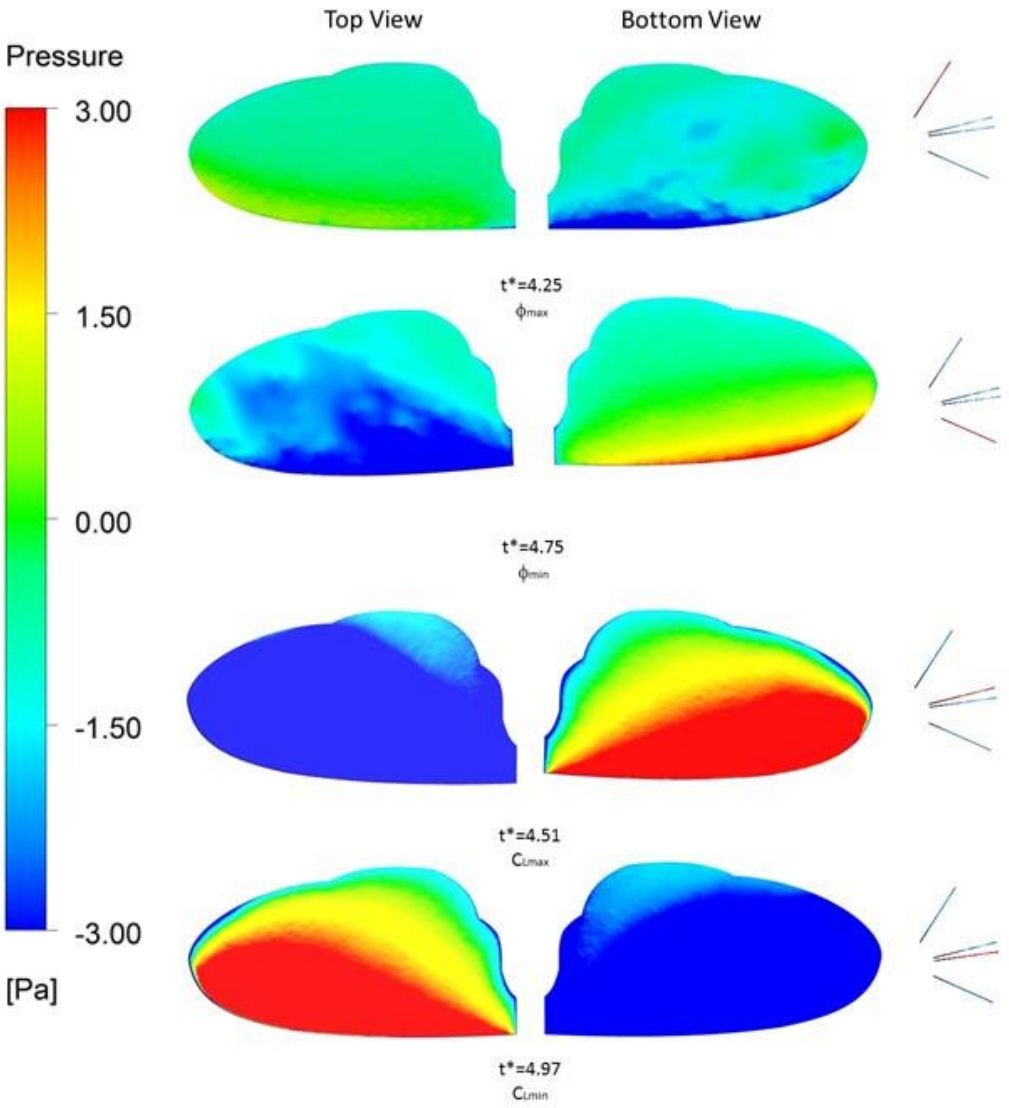

Figure 5. 21 Gauge static pressure (P-P∞) at the top and bottom surface of the wing at ϕ_{max}, ϕ_{min}, C_{Lmax} and C_{Lmin} positions at 4th period for forward-flight (case 2).

Figure 5.22 shows the x-vorticity (left) and the z-vorticity (right) distribution for one period at forward-flight. Blue regions indicate positive vorticity (CCW) and red regions indicate negative vorticity (CW). In the x-vorticity distribution the positive vorticity occurs upper surface of the wing; on the other hand, the negative vorticity occurs bottom surface. The majority of the vorticity improves on the bottom surface of the wing at the mid-upstroke (t*=4); on the other hand, the majority of the vorticity improves on the upper surface of the wing at the mid-downstroke (t*=4.5). In the z-vorticity distribution, positive vorticity is bound to the wing's root at mid-upstroke; on

the other hand, positive vorticity is bound to the wing's tip at mid-downstroke, the positive vorticity side displaced from the root to the tip when the flap direction changes. Different from hover mode, in forward flight mode, in the z-vorticity distribution, vorticities go to from the leading edge to the trailing edge because of the wind velocity.

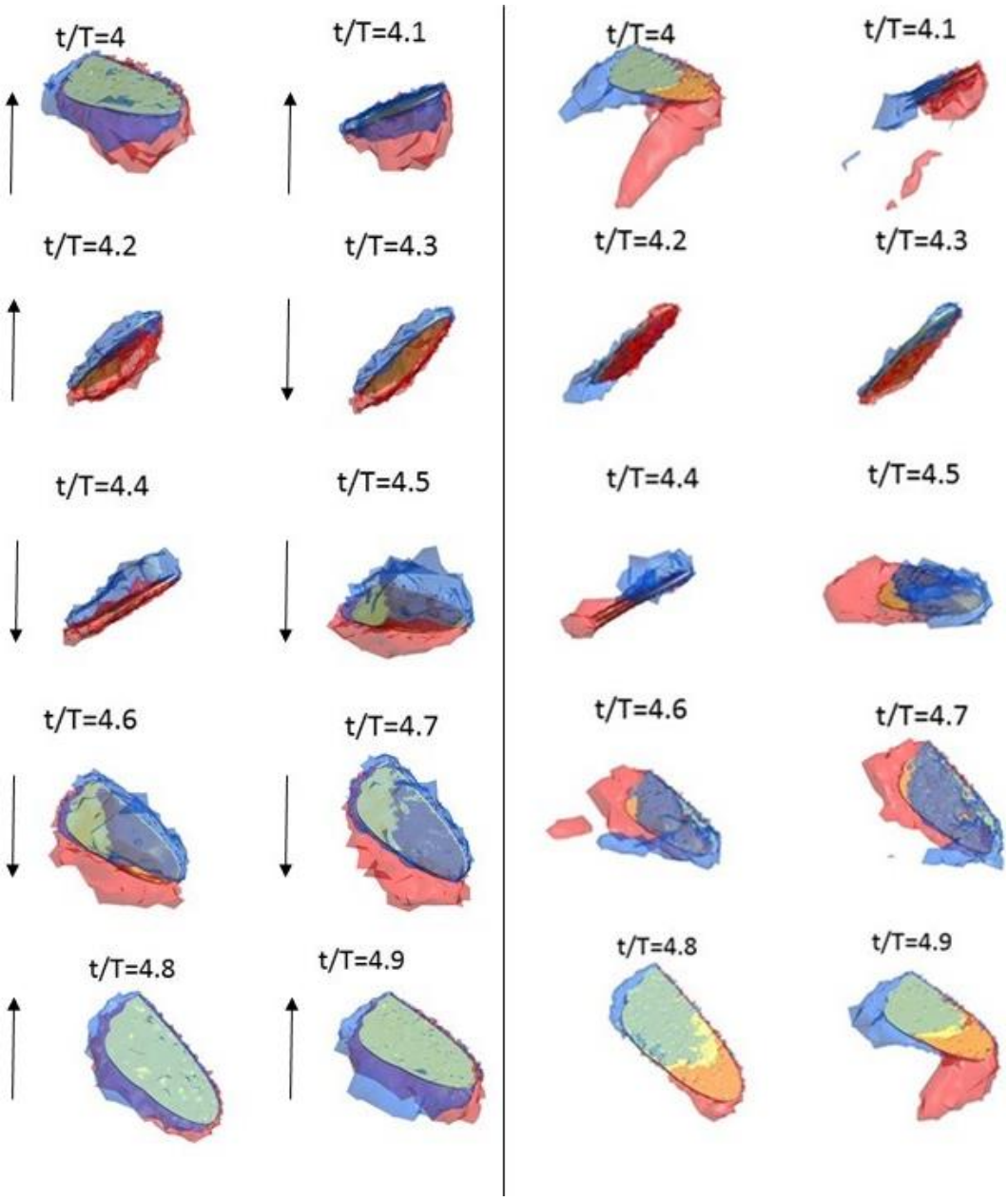

Figure 5. 22 Iso-surfaces of x-vorticity (left) and z-vorticity (right) at different time instances during 4th period for forward-flight (case 2)

5.7 Discussions for Numerical Analysis

The following points are considered after the analysis of the numerical simulations

- The positive lift is generated throughout the downstroke while the negative lift is generated throughout the upstroke.
- In lift coefficient plots, a single large peak is observed in one period.
- In drag coefficient plots, two peaks occurs in one period.
- The vortices cause a low pressure region on the upper side of the wing which is the suction side of the wing at C_{Lmax} position (approximately half-downstroke); on the other hand, the vortices cause a high pressure region in the bottom side of the wing.
- The vortices create a low pressure region in the bottom side of the wing which is the suction side of the wing at C_{Lmin} position (approximately half-upstroke); on the other hand, the vortices create a high pressure region in the upper side of the wing.
- Magnitude of the vortices at the tip is bigger than vortices at the root in hover cases that is tip vortices have a crucial role. Strong vortices originates near the tip.
- According to z-vorticity, in hover case, vortex sheds from the wingtip; on the other hand, in forward-flight case, vortex sheds from the trailing edge.
- In general, for hover cases, negative drag (thrust) occurs; on the other hand, positive drag (thrust) occurs in forward-flight cases.
- In hover cases, when flapping angle is 41.5° at 11.2 Hz flapping frequency, lift coefficient is between ±5; on the other hand, when flapping angle is 85.9° at 5.85 Hz flapping frequency, lift coefficient is between ±3.
- In forward-flight cases, the wind velocity is 3 m/s. when flapping angle is 85.9° at 5.85 Hz flapping frequency, lift coefficient is between ±6.
- For case 2, the lift coefficient at forward-flight case is twice as big as the lift coefficient at hover case.
- For case 2, magnitude of the gauge static pressure at forward-flight case is larger than the one at hover case.

CHAPTER 6

CONCLUSION

6.1 General Conclusions

In this thesis, flapping wing four-bar mechanism is designed, fabricated and tested experimental results are compared with numerical solutions. In the first part of this study, motor-driven and piezo-driven four-bar mechanism literature survey are done in order to understand their working principles. A single-degree of freedom double rocker four-bar linkage system kinematic analysis is introduced for the equation of motion of flapping wing. After kinematic analysis, 3D drawing of system is drawn by using Solidworks program. A fabrication process and experimental setup are also introduced.

Tests are conducted for different cases. Input angle is 10° in first case, while it is 20° in second case. As a result of the design of four bar mechanism when input angle is 10°, the flapping angle (ϕ) is 41.5° at 11.2 Hz flapping frequency. The maximum flapping deflection of the current mechanism is found to be 85.9° with 20° input angle and the flapping frequency attained with the servo motor is 5.85 Hz. Force and moment measurements are performed for all cases by using the 3 DOF sensor. All results are analyzed and post-processed with the MATLAB code develop by the authors. The net force and inertial force are found. The inertial force is calculated with two method: calculation method and measured method. In order to find the aerodynamic force, the inertial force is subtracted from net force and consequently results of measured aerodynamic force are similar to numerical analysis results.

CFD analysis is also performed to visualize instantaneous aerodynamic forces. Using dynamic mesh option, flapping motion is governed by UDF. Mesh refinement and time step size refinement are implemented. CFD results are visualized through the processor. Thrust force is generated in hover cases and drag force is generated in forward-flight cases. Approximately zero lift force is obtained.

CFD results and experimental force measurements are compared. There are some difference between experimental and numerical results. These difference could also originate from mechanical imperfections and mechanical uncertainty.

In conclusion, mechanism motion trajectory and kinematic parameters such as flapping frequency and flapping amplitude are important parameters that affects aerodynamic forces.

6.2 Future Studies

In the future study, new and more efficient four-bar mechanism will be designed. It is planned that the new mechanism is activated by a piezoelectric actuator. It is recommended to try different wing motions with different flapping angles. It is also targeted to design and fabricate rigid and flexible wing with different aspect ratios.

REFERENCES

[1] McMichael, J. M., Francis, M.S., Micro Air Vehicles-Toward a New Dimension in Flight, http://fas.org/irp/program/collect/docs/mav_auvsi.htm , [last visited on November 2015].

[2] Leonardo Da Vinci inventions http://www.da-vinci-inventions.com/flying-machine.aspx , [last visited on November 2015].

[3] Söylemez E., *Mechanism, 4th Edition*, Middle East Technical University, 2013.

[4] Pornsin-Sirirak, T. Tai, Y. Nassef, H. Ho, C. Titanium-alloy mems wing technology for a micro aerial vehicle application, *Journal of Sensors and Actuators A:Physical*, 2001, 89, 95-103.

[5] Bejgerowski, W. Ananthanarayanam, A. Mueller, D. Gupta, S.K. Integrated product and process design for a flapping wing drive-mechanism, *ASME Journal of Mechanical Design*, 2009, 131, 061006.

[6] Takahashi, H. Aoyama, Y. Ohsawa, K. Tanaka, H. Iwase, E. Matsumoto, K. Shimoyama, I. Differantial pressure measurement using a free-flying insect-like ornithopter with an mems sensor, *Bioinspirarion and Biomimetics*, 2010, 5, 036005 (7pp).

[7] Sahai, R. Galloway, K.C. Karpelson, M. Wood, R.J. *A flapping-wing micro air vehicle with interchangeable parts for system integration studies*, IEEE/RSJ International Conference on Intelligent Robots and Systems, 2012.

[8] Yılmaz, A., Design and development of a flapping wing micro air vehicle, MSc. Thesis, 2010.

[9] Seshadri, P., Benedict, M., Chopra, I., Understanding micro air vehicle flapping-wing aerodynamics using force and flowfield measurements, *Journal of Aircraft*, Vol. 50, No. 4, July-August 2013.

[10] Nguyen, Q. V., Chan, W. L. Debiasi, M. Design, fabrication and performance test of a hovering-based flapping-wing micro air vehicle capable of sustained and controlled flight, *IMAV* 2014.

[11] Mayo, D. B., Lankford, J.L., Benedict, M., Chopra, I. Experimental and computational analysis of rigid flapping wings for micro air vehicles, *Journal of Aircraft*, Vol. 52, No. 4, July-August 2015.

[12] Horsley, E.L. Foster, M.P. Stone, D.A. *State-of-the-art piezoelectric transformer technology*, EPE 2007.

[13] Fearing, R.S., Chiang, K.H., Dickinson, M.H., Pick, D.L., Sitti, M., Yan, J., "Wing transmission for a micromechanical flying insect." *IEEE Int. Conf. Robotics and Automation*, 2000.

[14] Cox, A., Monopoli, D., Cveticanin, D., Goldfarb, M. and Garcia, E.2002. ''The Development of Elastodynamic Components for Piezoelectrically Actuated Flapping Micro-air Vehicles,'' *Journal of Intelligent Material Systems and Structures*, 13:611-615.

[15] Syaifuddin, M., Park, Yoon, J. K., Goo, N.S., "Design and evaluation of LIPCA-actuated flapping device" *Smart Structures and Materials*, Vol. 5764, 2005.

[16] Syaifuddin, M., Park, H.C., Lee, S.K., Byun, D.Y., "An improved flapping wing system actuated by the LIPCA" *Smart Structures and Materials*, Vol. 6173, 2006.

[17] Nguyen, Q.V., Park, H.C., Goo, N.S., Byun, D.Y., "Aerodynamic force generation of an insect-inspired flapper actuated by a compressed unimorph actuator" *Chinese Science Bulletin*, 2009.

[18] Truong, Q.T., Nguyen, Q.V., Park, H.C., Byun, D.Y., Goo, N.S., "Modification of a four-bar linkage system for a higher optimal flapping frequency" *Journal of Intelligent Material Systems and Structures*, January 2011.

[19] Nguyen, Q.V., Park, H.C., Byun, D.Y., Goo, N.S., Yoon, K.J., "Characteristic of an insect mimicking flapping system actuated by a unmorph piezoceramic actuator." *Journal of Intelligent Materials Systems and Structures*, 19:1185-1193.

[20] Anderson, M. L., Sladek, N.J., Cobb, R. G., "Design, Fabrication and Testing of an Insect Sized MAV Wing Flapping Mechanism" *AIAA* January, 2011.

[21] Lindholm, G.J. Closed-loop control of constrained flapping wing micro air vehicle, Air Force Institute of Technology, PhD Thesis, March 2014.

[22] http://www.ati-ia.com/products/ft/ft_models.aspx?id=Nano17 [Last visited on 15.01.2016]

[23] Alford L. D. Jr. Aerodynamic Analysis of Natural Flapping Flight Using aLift Model Based on Spanwise Flow, PhD Thesis, May 2010.

[24] Shyy, W., Aono, H., Kang, C. Liu, H., *An introduction to flapping wing aerodynamics*, Cambridge University Press, 2013

[25] Matlab R2014a

[26] *Fluent v.14 User's Guide*.

[27] *ANSYS CFX User Guide*, ANSYS Inc.

[28] "ANSYS", [Online]. Available: http://www.ansys.com/ [Last visited on 12 June 2015].

[29] Versteeg, H.K., Malalasekera, W. *An Introduction to Computational Fluid Dynamics, Second Edition*, Pearson, 2007.

[30] Ellington, C.P. The Novel aerodynamics of insect flight: applications to micro air vehicles. *The Journal of Experimental Biology* 202, 3439-3448, 1999

[31] Hong, Y., Altman, A., Lift from Spanwise Flow in Simple Flapping Wings. *Journal of Aircraft*, Vol. 45, No.4, July-August 2008.

[32] Senol, M.G., Comez, Y.F., Kurtulus, D.F., Arikan, K.B., Testing of Flapping Wing Four-Bar Mechanism, Workshop on Non-Intrusive Measurements for unsteady flows and aerodynamics, October, 2015.